Micro- and Nanofabrication of Flexible Bioelectronic Interfaces

Hanna Karlsson-Fernberg

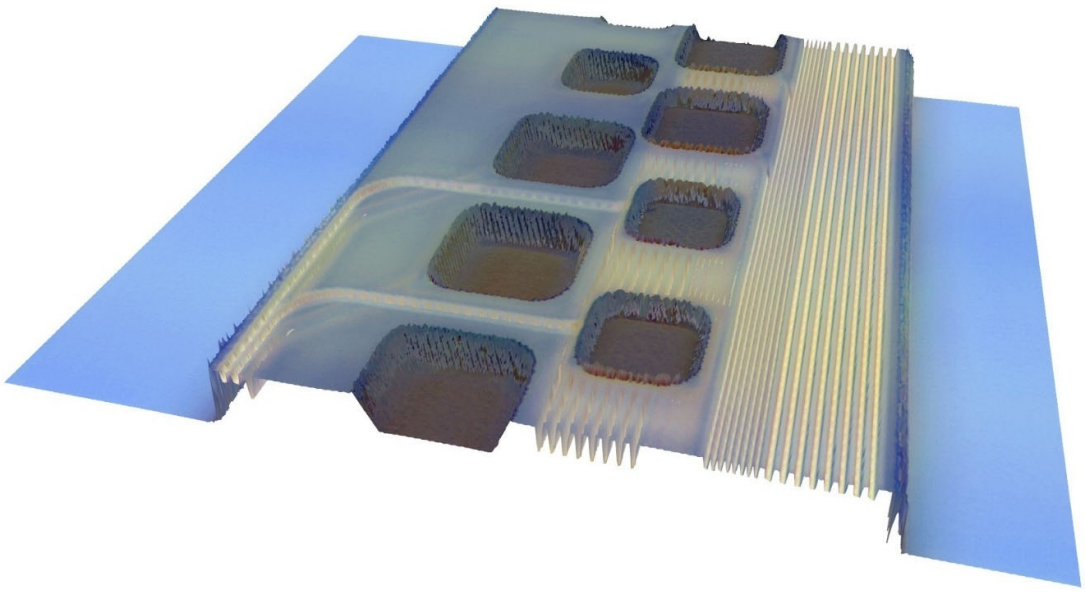

Chalmers University of Technology

Department of Microtechnology and Nanoscience – MC2

Electronic Materials and Systems Laboratory

SE-412 96 Göteborg, Sweden

Telephone +46 (0)31 772–1000

Licentiatavhandlingar vid Chalmers tekniska högskola

ISSN 1652–0769

Technical report no MC2–2026–480

THESIS FOR THE DEGREE OF LICENTIATE OF ENGINEERING

Micro- and Nanofabrication of Flexible Bioelectronic Interfaces

Hanna Karlsson-Fernberg

CHALMERS

Department of Microtechnology and Nanoscience (MC2)

Electronic Materials and Systems Laboratory

CHALMERS UNIVERISTY OF TECHNOLOGY

Gothenburg, Sweden 2026

Micro- and Nanofabrication of Flexible Bioelectronic Interfaces

Hanna Karlsson-Fernberg

Technical report no MC2–2026–480

ISSN 1652–0769

Chalmers University of Technology

Department of Microtechnology and Nanoscience – MC2

Electronic Materials and Systems Laboratory

SE-412 96 Göteborg, Sweden

Telephone +46 (0)31 772–1000

Cover: A magnification of a fabricated TIME device. More information can be found in Section 3.5. Credit: Ruggero Verre.

Micro- and Nanofabrication of Flexible Bioelectronic Interfaces

Hanna Karlsson-Fernberg

Department of Microtechnology and Nanoscience – MC2

Chalmers University of Technology

Abstract

Flexible neural interfaces represent a promising platform for the treatment of neurological disorders, enabling the restoration of motor function and communication through targeted electrical interaction with neural tissue. These devices are typically fabricated on polymeric substrates such as polyimide (PI) or Parylene C, with thin-film metal interconnects and electrode materials like iridium oxide. Increasing channel density and spatial resolution requires miniaturization, which in turn demands advanced micro- and nanofabrication techniques. This thesis investigates fabrication strategies for high-density flexible neuroelectronic implants, with a focus on reducing feature and implant size while maintaining electrical performance and structural integrity. Electron-beam lithography (EBL) is employed to pattern sub-micrometer interconnects on polymer substrates. While EBL is well established for nanoscale patterning, its application to polymer-based systems remains underexplored; this work addresses this gap by evaluating process limitations and optimization strategies. The electrical and electrochemical implications of nanoscale features are systematically studied, including interconnect resistance, electrode behavior, and the role of conductive materials and adhesion layers. In addition, fabrication approaches for high-aspect-ratio vias and multilayer architectures are developed to enable increased channel density without significantly increasing implant volume. Finally, multilayer devices with nanoscale features are fabricated to demonstrate the feasibility of EBL on PI substrates and to assess the performance of miniaturized interconnects and electrodes in neural interfaces. Overall, this work identifies key limitations in the miniaturization of flexible bioelectronic interfaces and provides fabrication strategies to improve their scalability and manufacturability, contributing to the development of high-density, chronically implantable neural devices.

Keywords: neurotechnology, bioelectronics, nanofabrication, miniaturization, polymeric materials, flexible electronics

List of publications

Paper A is based on the work in this thesis:

A. Towards High-Resolution Polymeric Neural Interfaces: A Practical Guide for Electron Beam Lithography

Hanna Karlsson-Fernberg and Maria Asplund

Submitted, 2026

Other contributions

Paper: Covalent Binding of Dexamethasone to Polyimide Improves Biocompatibility of Neural Implantable Devices

Giulia Turrin, José Crugeiras, Chiara Bisquoli, Davide Barboni, Martina Catani, Bruno Rodríguez-Meana, Rita Boaretto, Michele Albicini, Stefano Caramori, Claudio Trapella, Thomas Stieglitz, Yara Baslan, **Hanna Karlsson-Fernberg**, Fernanda L Narvaez-Chicaiza, Edoardo Marchini, Alberto Cavazzini, Ruben López-Vales, Maria Asplund, Xavier Navarro, Stefano Carli.

Advanced Healthcare Materials 2025, 14, 2405004. https://doi.org/10.1002/adhm.202405004

Paper: A novel inflammasome inhibitor reduces the foreign body reaction against neural implants

Jose Crugeiras, Giulia Turrin, Chiara Bisquoli, María Rodríguez-Brañas, Bruno Rodríguez-Meana, Tiziano De Ventura, Neus Hernández, Jessica Jaramillo, Alice Honovich, Ignacio Delgado-Martínez, Natalia Lago, **Hanna Karlsson-Fernberg**, Maria Asplund, Stefano Carli, Claudio Trapella, Xavier Navarro,

Submitted, 2026

Paper: Sputtered iridium oxide film (SIROF) for on-chip micro-energy storage applications

Qi Li, Lukas Matter, Muhammad Hassan, R.K. Azega, **Hanna Karlsson-Fernberg,** Björn Wickman, Johan Liu, Maria Asplund, Per Lundgren, Mazharul Haque

Journal of Energy Storage, 161, 2026, 121720, https://doi.org/10.1016/j.est.2026.121720.

Paper: Incorporation of RF Magnetron Sputter-deposited Silicon Caride Films Enhances Longevity of Polyimide Thin-Film Electrodes

Lukas Matter, Kenneth A. Fluker, **Hanna Karlsson-Fernberg**, Gonzalo León, Jack W Judy and Maria Asplund

Manuscript, 2026

Process notes: Polyimide Handbook

Lukas Matter, **Hanna Karlsson-Fernberg**, Karin Hedsten

List of acronyms

CNS: Central nervous system

PNS: Peripheral nervous system

FBR: Foreign body reaction

LIFE: Longitudinal intrafascicular electrode

TIME: Transversal intrafascicular multichannel electrode

EA: Electrode array

SIROF: Sputtered iridium oxide film

CSC: Charge injection capacity

CIC: Charge injection capacity

PI: Polyimide

PDMS: Polydimethylsiloxane

CVD: Chemical vapor deposition

LCP: Liquid crystal polymer

EBL: Electron beam lithography

PVD: Physical vapor deposition

RIE: Reactive ion etching

ICP-RIE: Inductively coupled plasma reactive ion etching

SEM: Scanning electron microscopy

XPS: X-ray photoelectron microscopy

CV: Cyclic voltammetry

EIS: Electrochemical impedance spectroscopy

Contents

Introduction

Neural interface technologies, or neuroprosthetics, are medical devices that have emerged over the past three decades with the potential to treat a wide range of disorders affecting the central and peripheral nervous systems[1,2]. These devices are currently used to manage conditions such as Parkinson's disease, epilepsy, paralysis, severe depression, and chronic pain[2–5]. They have also achieved clinical success in restoring hearing through cochlear implants[6] and show strong potential for restoring sensory and motor function[7], as well as vision[8]. Bioelectronic medicine utilizes such technologies to modulate neural activity through direct interaction with the nervous system[9]. Beyond conventional stimulation and recording, modern neural interfaces enable bidirectional communication with neural tissue, which is essential for advanced applications such as brain–machine interfaces (BMIs)[10] and brain–computer interfaces (BCIs) [1]. In these systems, neural interfaces can enable direct control of external devices, such as, for instance, robotic prostheses, or to restore communication in patients with severe paralysis[10,11].

The development of chronically implantable neural devices has increasingly relied on flexible polymer substrates, including polyimide (PI), Parylene C, SU-8, and PDMS[12–15]. These materials provide mechanical compliance that better matches the properties of soft tissue, improving biocompatibility and reducing adverse tissue responses, thereby supporting long-term implantation[2,16]. Further improvements in biocompatibility can be achieved through miniaturization, which reduces the implant footprint and the size of critical features[17]. At the same time, increasing the number of recording and stimulation channels enhances spatial resolution, which is crucial for high-performance BMI and BCI systems[1,18,19].

Modern flexible neuroelectronic implants are typically fabricated using thin-film technologies, where functional layers are sequentially deposited and patterned using micro- and nanofabrication processes[20]. These include lithographic techniques, physical vapor deposition (PVD) methods such as evaporation and sputtering, and various etching processes. While optical lithography has traditionally been used for device patterning, recent work has explored EBL to achieve sub-micrometer feature sizes and higher interconnect densities[13]. However, despite its maturity as a nanoscale patterning tool, there are still limited date for patterning with EBL on polymer-based substrates. Challenges specific to these materials include substrate charging, thermal effects, and non-planarity, all of which potentially complicate process reliability and resolution[13].

Against this background, a key question is which factors fundamentally limit the miniaturization of neuroelectronic devices when using EBL-based fabrication on polymeric substrates. Addressing this question is essential for enabling further scaling of channel density without compromising electrical performance or long-term reliability.

This thesis therefore investigates fabrication strategies for increasing channel density in flexible neuroelectronic implants while minimizing device footprint, with a particular focus on identifying and overcoming the limiting factors associated with sub-micrometer patterning on polymer substrates. The work explores EBL to define nanoscale interconnects, as well as the selection and optimization of conductive materials to improve electrical performance. As feature sizes decrease, additional challenges arise, such as reduced adhesion of thin-film metals due to limited contact area with the substrate.

To further increase channel density, multilayer metallization strategies are explored, where interconnects are routed across multiple layers and electrically connected through via structures or by placing the electrodes in different layers. Fabrication of such infrastructure requires hard-mask-based etching processes, adding complexity to the process flow. In this work, different via fabrication approaches are evaluated with the aim of reducing resistance and improving signal transmission.

Overall, this work seeks to advance the field of neuroprosthetics by enabling the miniaturization and increased integration density of flexible neural interfaces through optimized micro- and nanofabrication techniques. By addressing key material and process limitations, the thesis contributes to the development of high-density, chronically implantable devices capable of reliable bidirectional communication with the nervous system, with applications in BMI and BCI technologies.

1 Background

1.1 The nervous system

The central nervous system (CNS) consists of the brain and spinal cord, located inside the skull and vertebral column[21]. The extension of the brain to the rest of the body is called the peripheral nervous system (PNS)[22]. The location of CNS and PNS in the human body are shown in Figure 1.

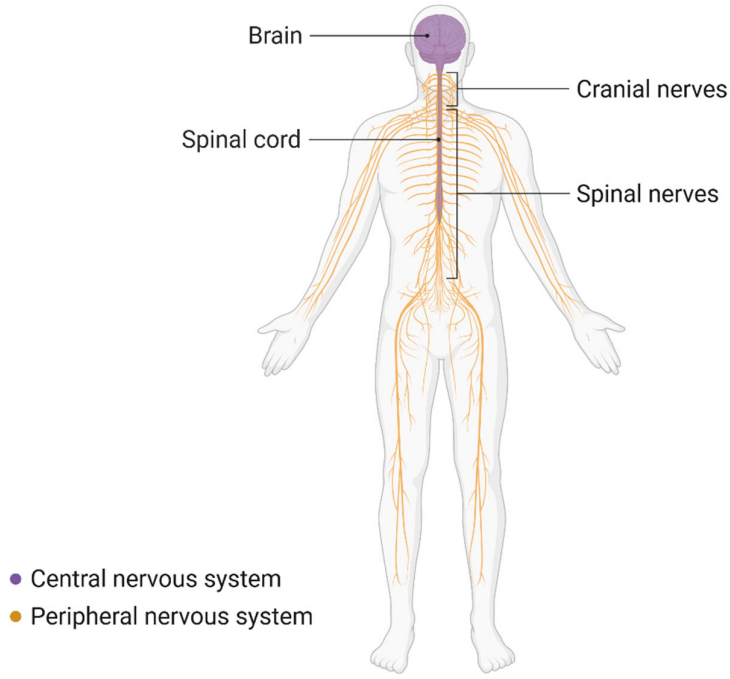

Figure 1. The major components of the nervous system. It consists of the central nervous system consisting of the brain and spinal cord (shown in purple) and the peripheral nervous system (shown in yellow). Created in BioRender.

The brain integrates sensory input, coordinates motor output and handles higher cognition like thinking, memory, emotion and decision making[23]. The spinal cord is the mediator between the brain and the periphery, and transmits sensory information as well as descending motor commands from the brain to control muscles and control the body's autonomic function[24]. The PNS is divided into the somatic nervous system and the autonomic nervous system. The somatic nervous system manages voluntary actions and transmits sensation such as touch, pain and temperature to the CNS, and the motor fibers command skeletal muscles[25]. The autonomic nervous system controls involuntary processes such as heart rate, digestion and glandular

secretion. It includes the sympathetic nervous system that governs stress response, and the parasympathetic nervous system that governs restoration[26].

The brain consists of neurons and non-neuronal cells[23]. The role of the non-neuronal cells is to support the function of the neuronal cells, with for example oxygen and nutrients or insulation[23]. The brain consists of gray and white matter: the gray matter mainly consists of neurons and white matter consists of the axons, which are myelinated for optimal electrical conduction[23].

1.1.1 Neuronal communication

Neuronal cells (neurons) are the fundament of the nervous system, and they communicate chemically or electrically[23]. The neuron consists of a cell body, with a nucleus and dendrites that extend from the cell body highly branched. From the cell body there is an extension called an axon. The axon, similarly, to the dendrites are highly branched. The neurotransmission occurs in the axon, and the signal is picked up by the dendrites on a nearby cell, forming large electrical network[27]. The neuron anatomy is shown in Figure 2.

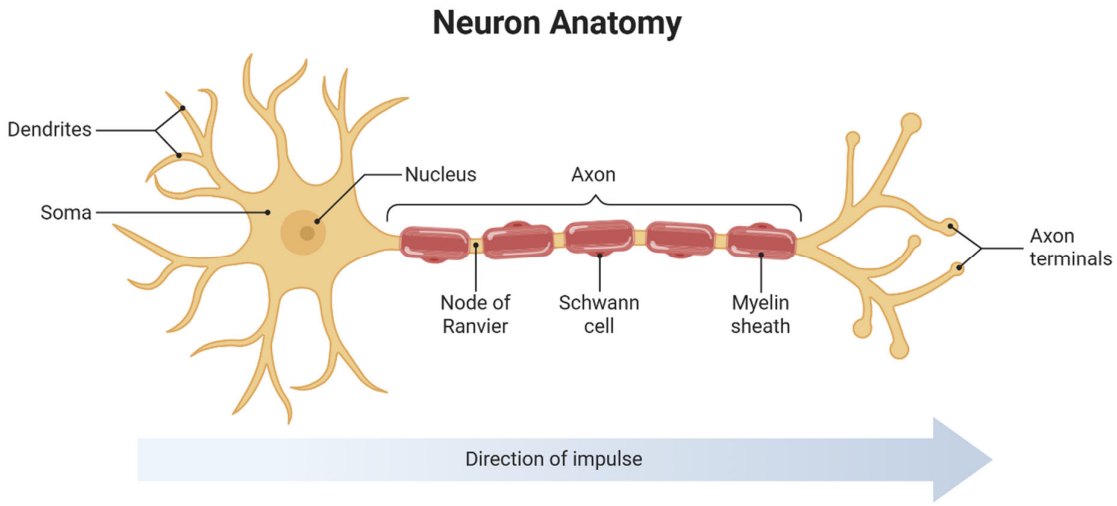

Figure 2. The anatomy of the neuron, consisting of the soma which contains the nucleus, extension from the soma, dendrites, the axon and axon terminals, where the synapse is located. Created in BioRender.

Communication occurs through the small gap between the axon and dendrite, called synapse[23]. It starts with the generation of the action potential caused by an influx of ions across the cell membrane, inducing a difference in the ion concentration inside and outside the cell[27]. The

action potential travels down the axon to the terminal. For electrical synapses there is a gap junction that links the presynaptic neuron i.e. the neuron sending the signal, to the postsynaptic neuron i.e. the neuron receiving the signal[23,27]. The electrical signal is transmitted by ions traveling through small channels. For chemical synapses, when the action potential arrives at the axon terminal, there is a rapid influx of Ca^{2+} ions from outside the cell[27]. The rise in Ca^{2+} concentration causes neurotransmitter filled vesicles to fuse with the cell membrane and release its content in the gap between the presynaptic neuron and the postsynaptic neuron[27]. This phenomenon is called exocytosis. The neurotransmitters can then bind to receptors on the postsynaptic neuron, activating or deactivating the neuron. Electrical and chemical synapses are shown in Figure 3.

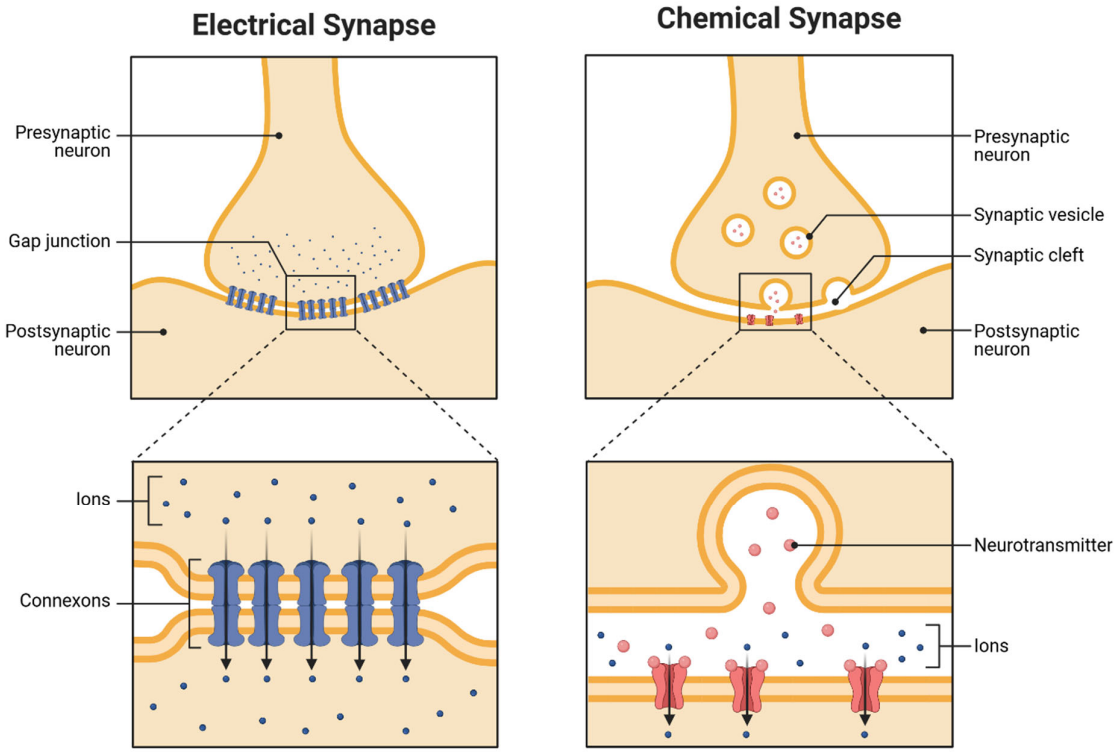

Figure 2. Schematic of electrical and chemical synapse. Figure created in BioRender.

1.1.2 The nerve

The PNS consists of nerves which are cord-like bundles of axons that transmit the electrical impulses from the brain to the rest of the body. The nerve tissue are many parallel axons from multiple neurons that extend all the way from the brain out to the limbs or organs, and thus can reach over a meter in lengths[28]. Peripheral axons are wrapped by myelin formed by Schwann cells, which increases signal conduction velocity[29]. Each axon is surrounded by endoneurium,

which contains capillaries that help supply oxygen and nutrients[30]. Axons are grouped into fascicles surrounded by perineurium, and the entire nerve is enclosed by epineurium, which also contains blood vessels. A cross section of a nerve is illustrated in Figure 4a.

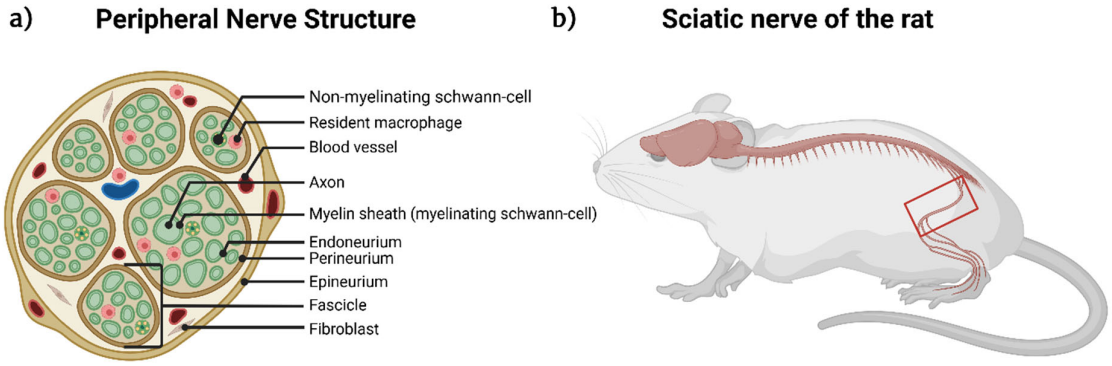

Figure 4. a) The structure of the peripheral nerve. Each axon is surrounded by myelin sheath for insulation and endoneurium for oxygen and nutrient supply. Several axons are bundled up together forming a fascicle which is surrounded by perineurium. Each nerve consists of several fascicles and contain blood vessels and cells like macrophage, fibroblasts and non-myelinating Schwann cells. b) The placement of the sciatic nerve of the rat marked in the red rectangle. Figure created in BioRender.

Human peripheral nerves vary considerably in size depending on their location and function[31]. Small cutaneous nerves can measure less than 1 mm in diameter, whereas large mixed nerves such as the median and ulnar typically range from about 3 to 6 mm[31]. The sciatic nerve of the rat (shown in Figure 4b) serves as a widely adopted preclinical model for peripheral nerve research due to its accessibility, well-characterized anatomy, and functional relevance to human neuropathies[32]. It is approximately 1 mm wide[33,34].

1.2 Foreign body reaction and biocompatibility

Foreign body reaction (FBR) is the reaction when a non-degradable material is implanted or inserted into the tissue, following a well-defined sequence and typically ends in a fibrotic encapsulation[35,36]. The FBR cascade differs whether an object is implanted into the PNS and CNS, but as this thesis is focused more on PNS implant, the cascade for PNS is described here and illustrated in Figure 5.

1. *Injury and blood contact:* The implantation or penetration of the object causes tissue damage and bleeding[35,36]. Blood and interstitial fluid wet the surface of the object and plasma proteins (e.g. albumin, fibrinogen, fibronectin) absorb to the surface forming a protein layer.
2. *Acute inflammation*: A cascade of damage-associated signals is triggered that recruit neutrophils and other immune cells[35,36]. Neutrophils adhere to the protein-coated surface and release enzymes and reactive oxygen species to phagocytose or degrade the object. Blood platelets and mast cells release signaling molecules, cytokines and chemokines that amplify inflammation and recruit monocytes. This usually lasts from minutes to days.
3. *Transition to chronic inflammation:* Monocytes differentiate to become macrophages and adhere to the protein-coated object[35]. Macrophages secrete cytokines, growth factors and proteolytic enzymes, sustaining an inflammatory environment at the interface. This stage usually lasts from days to weeks.
4. *Macrophage fusion creates foreign body giant cells*: The adhered macrophages fuse into multinucleated foreign body giant cells when they cannot degrade the material[35,36]. These cells spread over the surface of the object and secrete enzymes and reactive oxygen species that attempt to degrade the material. Together with the macrophages, the foreign body giant cells form a foreign body granuloma at the surface.
5. *Granulation tissue formation:* Fibroblasts and endothelial cells are recruited by macrophage-derived growth factors[35,36]. New tissue containing capillaries and fibroblasts develop around the object. In this stage the tissue goes from inflammatory to slowly healing.
6. *Fibrous encapsulation:* Fibroblasts deposit collagen and create an extracellular matrix, causing the granulation tissue to turn into a dense fibrous capsule around the object[35,36]. The foreign body giant cells and macrophages usually stay in a thin layer adjacent to the object.

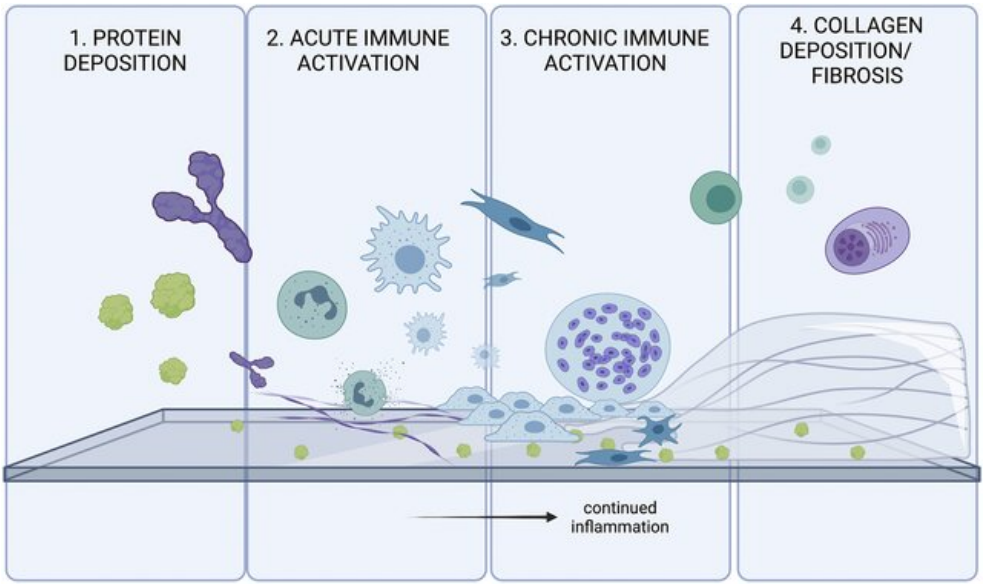

Figure 5. A simplified description of the foreign body reaction cascade, starting with protein deposition, followed by acute immune reaction, chronic immune activation and lastly collagen deposition/fibrosis. The figure is reprinted from Karkanitsa et.al. (2021) under CC BY 4.0.

1.2.1 Biocompatibility

Biocompatibility is defined as "a material's ability to perform its intended function in contact with a living system (e.g., a tissue) without causing any undesirable local or systemic effects, while supporting appropriate beneficial tissue response"[37,38]. Biocompatibility is highly context-dependent, and all implanted devices elicit an immune response, with varying response magnitude, despite being deemed biocompatible. To evaluate biocompatibility, standardized testing with ISO 10993 is usually performed, which examines the material through tests with cytotoxicity, sensitization, irritation and genotoxicity, to ensure no adverse reaction occurs toward the material[36,39].

Biocompatibility is further divided into structural biocompatibility and surface compatibility. Structural biocompatibility refers to the overall mechanical and physical compatibility of an implant's bulk material with surrounding tissues, ensuring it withstands physiological loads without deformation, fracture, or stress shielding that could lead to tissue resorption or inflammation[2,40]. It also includes matching the body's soft tissue modulus. Surface biocompatibility focuses on the implant's interface with biological environments, where

chemistry, topography, wettability, and protein adsorption dictate cell adhesion, bacterial resistance, and immune responses[2,41].

1.2.2 Biostability

Apart from biocompatibility, biostability is another important concept relating to the implant and its interaction with the surrounding tissue. Biostability refers to the material's chemical stability and system integrity when it is implanted into the body[2]. For instance, metals can easily corrode when they are implanted into the harsh environment of the body, and polymers can degrade, especially in an inflammatory environment following the implantation where there might be pH changes that can further degrade the material[2].

1.2.3 Foreign body reaction and neural devices

The FBR to implanted neural devices represents a primary challenge in achieving chronic functionality, culminating in a stable fibrotic encapsulation that spatially fixates the implant within the tissue[36,42]. Although this fibrotic capsule for implants is considered to provide mechanical stability on a general level, it is detrimental for neural interfaces as it drastically degrades device performance by increasing electrode-tissue impedance and attenuating signal-to-noise ratios for recording, while limiting charge injection capacity for stimulation due to the non-conductive interface between the devices and the tissue. These concepts are described in more detail in Section 1.3.

By implanting the devices close to the nervous tissue, a higher signal selectivity and signal-to-noise ratio can be achieved[43]. However, due to the high level of invasiveness of these implants, FBR is a major challenge, preventing long-term functionality and stability of these devices[44–46]. Factors affecting the severity of the FBR are implant stiffness, surface chemistry and coatings, surface topography, device geometry and size, and implantation method[36]. These are described here further.

Implant stiffness: Mechanical mismatch between neural implants and brain tissue is a major factor contributing to the FBR and subsequent scar tissue formation[38]. For neural devices it has been demonstrated that devices fabricated on flexible substrates exhibit a reduced FBR compared to those based on rigid silicon, particularly in chronic implantation[2].

For long-term implantation, close mechanical conformity between the implant and the surrounding tissue is essential, as the device is constantly subjected to micromotions within the tissue[44]. Persistent mechanical strain caused by such motion can lead to continuous local inflammation, ultimately exacerbating the severity of the FBR[44]. Materials used to mitigate this effect are described in Section 2.1.1.

Surface chemistry and topography: The surface chemistry greatly affects the protein adsorption and denaturation that initiates the cellular response[38]. By being able to control the amount and composition of protein adhering to the implant and the degree of protein spreading on the surface, causing exposure of inflammatory protein sequences that inflammatory cell adheres to[41], one can reduce the FBR and thus the thickness of the insulating fibrotic capsule[2]. By engineering the surface through changing the surface chemistry, wettability, surface composition and morphology the protein adsorption can be influenced and the following cellular response to the implant is altered[41]. Furthermore, the topography, including roughness at micro- and nanoscales, alters cell spreading and differentiation, integration of implant[38] and bacterial adhesion in the case of bacterial infection[47].

Surface charge also has an influence on protein adsorption and the interaction between the immune cells and implant material. It has been shown that implanted materials with negative response induce less FBR compared to materials with positive charge[38]. Moreover, it has been shown that hydrophobic surfaces favor protein adsorption energetically whereas hydrophilic surfaces have protein repellent characteristics[38].

Because the surface properties of the implant affect the FBR outcome, engineering strategies to reduce the FBR and improve implant integration have been explored. This includes binding in functional molecules to the surface[38], surface modification to attain negatively charged surfaces as well as hydrophilic surfaces[38], altering surface topography etc[48]. Additionally, binding in a drug to the surface of an implant has been tested, and showed positive results as described in Paper Covalent Binding of Dexamethasone to Polyimide Improves Biocompatibility of Neural Implantable Devices[42] and A novel inflammasome inhibitor reduces the foreign body reaction against neural implants presented as Other contribution in this thesis.

Device geometry and size: Geometry and size strongly affect the FBR outcome after implantation of the device, by changing how the immune cells and tissue mechanically and spatially interact with the implant surface[38]. It has been shown that larger, bulker implants

evoke a stronger FBR compared to smaller implants, resulting in thicker fibrotic capsules. However, this effect might also be due to increased stiffness of the object and not the size[38,49].

The shape is equally important as it has been shown that sharp objects elicit a higher FBR, possibly due to higher interfacial stress. For example, spherical and circular objects have shown to result in lower FBR compared to discoidal objects[38].

Implantation method: Insertion trauma can cause bleeding and significantly contribute to scarring[38]. Hence, an implantation with less trauma can be critical to reduce inflammation post implantation. The stiff probes are associated with less insertion trauma in the brain compared to flexible probes that require a shuttle for insertion[49,50]. Moreover, blood deposits in the brain can also be problematic, although it's generally not problematic in other tissues[50].

1.3 Neuromodulation

Neuroprosthetics uses neuromodulation to target the nervous tissue through alteration of nerve activity by delivery of a stimulus, such as electrical, chemical or other stimulation[51,52]. To effectively inject impulses into the nervous tissue, important characteristics of the electrode material is low impedance and stability over billions of pulses to ensure safe, efficient modulation at kHz frequencies[9,53]. The impedance of the electrodes must be low to allow the charge to transfer from the electrode to the tissue. Impedance is the total opposition (measured in Ohms, Ω) to alternating current flow at the electrode-tissue interface, comprising resistance and reactance. When recording neural signals, impedance acts as a gatekeeper for signal quality: low impedance ensures clear, low-noise recordings, while high impedance attenuates signals and increases noise[9,54].

The most common method for injecting charge into the tissue is to use two-phase balanced charge electric pulses that inject the same amount of charge in the anodic and cathodic phase, resulting in a net zero charge[55]. Important concepts regarding the electrode material that is used for stimulation are charge injection capacity (CIC) and charge storage capacity (CSC). Maximum CIC is the amount of charge an electrode can deliver to an electrolyte or tissue during a stimulation pulse without causing irreversible electrochemical reactions, such as water electrolysis and other chemical reactions resulting in chemical species that can damage the tissue[56,57]. In neural stimulation, it is usually reported as charge per unit area, for example $\mu C/cm^2$, giving how much charge a given electrode material can safely inject over one single pulse. CSC is the amount of charge an electrode can reversibly store over a given potential

window, usually measured from a cyclic voltammogram (described in Section 2.3.3.1) by integrating the current over voltage[55]. In practice, porous coatings, rough surfaces, and materials such as ruthenium oxide and iridium oxide (IrOx) show higher CSC than smooth noble-metal films[58] (described further in Section 2.1.2.1). Furthermore, for long-term implantation, high durability of the electrodes is extremely important as they are under continuous electrical load[59]. The applied voltage can cause unbalanced redox reactions which accelerate the corrosion on the electrode material.

1.3.1 Neuroprosthetics

Neuroprosthetics can be divided into CNS implants and PNS implants. Because this thesis is more focused on PNS implants, only a short overview of CSN implants is included.

1.3.1.1 CNS implants

CNS implants are microfabricated devices surgically inserted into the brain or spinal cord to interface with neural tissue for recording or stimulation. CNS implants can be divided into several main types based on where they are implanted and their function.

Deep brain stimulation implants are used to stimulate specific brain regions. These devices are commonly used to reduce symptoms such as tremor, rigidity, and slowed movement in disorders like Parkinson's disease, and is also used in some cases of epilepsy[60]. Cortical implants are placed on or in the surface of the brain and are mainly used to record or stimulate brain activity, often as part of BCIs systems that help people control external devices or communicate[61]. BCI implants focusses on decoding neural signals and translating them into commands for computers, prosthetic limbs, or speech devices[5]. Their main function is to support communication and movement in people with paralysis or severe motor impairment.

Spinal cord stimulators are implanted along the spinal cord and are mostly used to treat chronic pain by interrupting pain signals before they reach the brain[62] but are also explored to help people with spinal cord injury regain their body function[4].

Other CNS-related implants include auditory brainstem implants and other sensory prostheses[63,64]. These devices bypass damaged pathways and directly stimulate central neural structures to restore hearing or, in some cases, vision[6,15,63].

1.3.1.2 PSN implants

Peripheral nervous system (PNS) implants are microfabricated devices surgically or percutaneously interfaced with the peripheral nerve roots, or neuromuscular junctions to enable recording, stimulation, or neuromodulation of somatic or autonomic pathways. Additionally, PNS implants can be used to interface a bionic limb into the nervous system, requiring bidirectional communication with the nervous system. There are several types of nerve implants that vary in invasiveness.

The extraneural cuff implant are positioned around the nerve with electrodes on the inner side of the device, facing the nerve. Because of its placement, it will only be able to stimulate the outer part of the nerve and therefore only a few subgroups of nerve fibers, which is a limitation of these devices[65]. To improve this, the flat-interface nerve electrode was developed which slowly flattening to nerve into a ribbon-like shape, allowing to reach deeper fascicles of the nerve[65,66]. The advantage of the extraneural devices is that they are easy to handle compared to other, more invasive variants that require implantation into the nerve. There are long-term data showing that cuff electrodes can be stable and function more than 10 years[66].

To improve signal selectivity and signal-to-noise ratio, the PNS implants can be implanted inside the nerve[65]. Slightly more invasive is the slowly penetrating interfascicular nerve electrode that is inserted into the epineurium, but outside of the nerve fascicle[67]. A similar implant is the flexible nerve plate, which is a thin flexible double-sided PI-based device that is inserted into the epineurium[68].

Implanting electrodes directly into nerve fascicles increases invasiveness compared to extraneural approaches. However, this intrafascicular placement enables direct contact with individual nerve fibers, thereby enhancing signal selectivity and signal-to-noise ratio[43].

The longitudinal intrafascicular electrode (LIFE) is, as the name suggests, implanted longitudinally, targeting individual fascicules[65,69]. The LIFE implant is thin nerve electrodes inserted along the length of the nerve to provide selective stimulation and recording from specific axon populations. They are designed to improve spatial selectivity for neuroprosthetic implants while remaining minimally invasive compared with larger nerve interfaces. Because they are placed inside the fascicle rather than around the whole nerve, LIFE implants can achieve better selectivity than cuff electrodes[69,70].

To cover a larger set of fascicles for each implant, the transversal intrafascicular multichannel electrode (TIME) was developed[65]. This device is implanted straight through the nerve, improving the contact with a large range of fascicles. The tight interface with the nerve tissue helps to produce more selective stimulation patterns for neuroprosthetic control or sensory feedback and thus, TIME implants were developed to improve spatial selectivity while keeping the implant small[66,70]. One example of the TIME design, the bent design that has been fabricated in the BioFINE project[71] are shown in Figure 6. The implant has electrodes on the two arms, which when folded provides contact between the electrodes and nerve on both sides of the devices. This TIME implant has an electrode array (EA) site width of 200 µm.

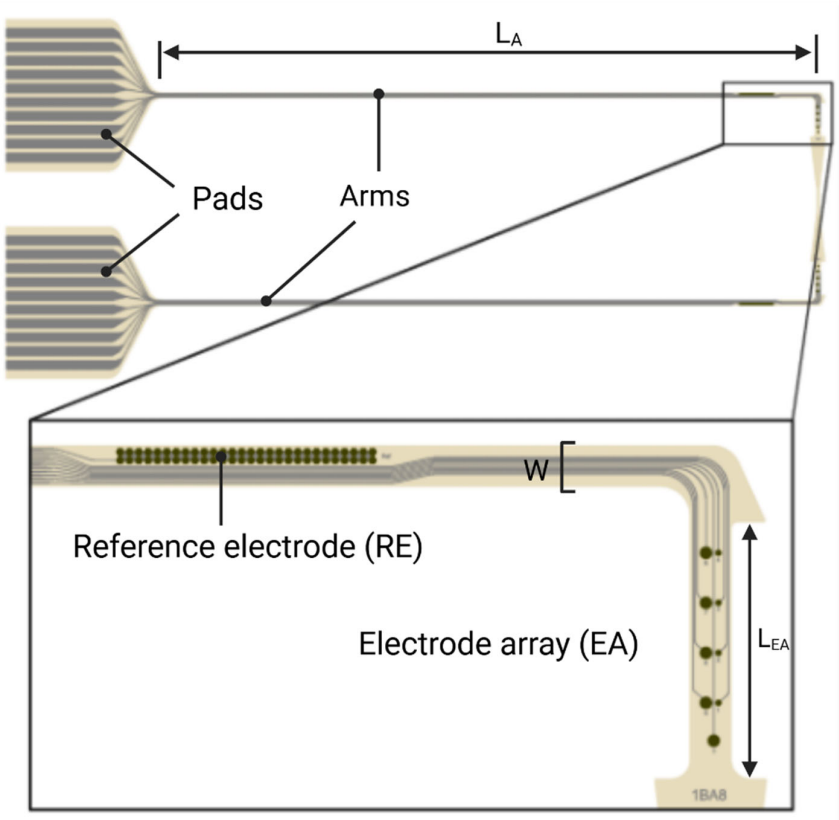

Figure 6. A bent TIME implant. The implant is folded and sewn into the nerve. The bent shape improves the stability of the implant in the nerve compared to the straight one. Dimensions of the implant is L_A=24.5 mm, L_{EA}=1 mm and W=0.2 µm.

Figure 7 shows how the implant is placed into the sciatic nerve of the rat using the sew-in technique. The electrode array site is about 1 mm wide, that corresponds to the width of the sciatic nerve of the rat (described in Section 1.1.2).

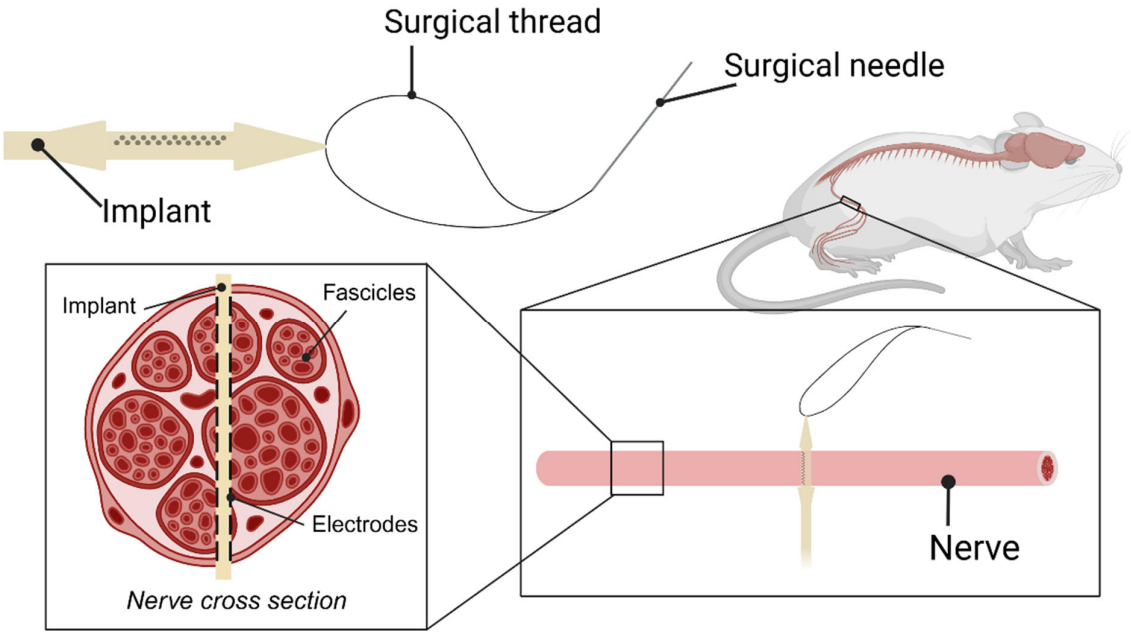

Figure 7. How the TIME implant is placed transversally in the nerve, interfacing the fascicles. The devices are sewn into the sciatic nerve of the rat. Figure created in BioRender.

To effectively test these devices in vivo, the implants are commonly evaluated using functional tests such electrophysiological, pain and locomotion testing of the rats as well as histological testing[45]. Electrophysiological testing can be performed by stimulating individual nerves and measuring muscle response, or by recording nerve activity[65,70].

2 Materials and methods

2.1 Materials

Flexible bioelectronic devices consist of polymer substrates, electrodes, conducting lines, a reference electrode and pads for external connection. This section describes the materials more in depth.

2.1.1 Polymers for neural implants

Polymers play an important role in biomedical engineering as flexible substrates, encapsulants, and structural components for implantable devices, offering tunable mechanical compliance to match the body's soft tissues and minimize chronic inflammation[2]. For example, the Youngs modulus of the brain tissue is around 1.9 kPa, whereas for many common polymeric thin-film substrate the modulus is around 2.5-2.9 GPa, and for silicon 179 GPa[59], proving higher mechanical compatibility of polymeric substrates compared to typical microsystems substrates. The chemical inertness, processability by spin-coating or chemical vapor deposition (CVD), and compatibility with microfabrication techniques made polymeric substrates highly suitable for flexible neural interfaces[2,13]. Some common polymers used for neural implants are shown in Figure 8.

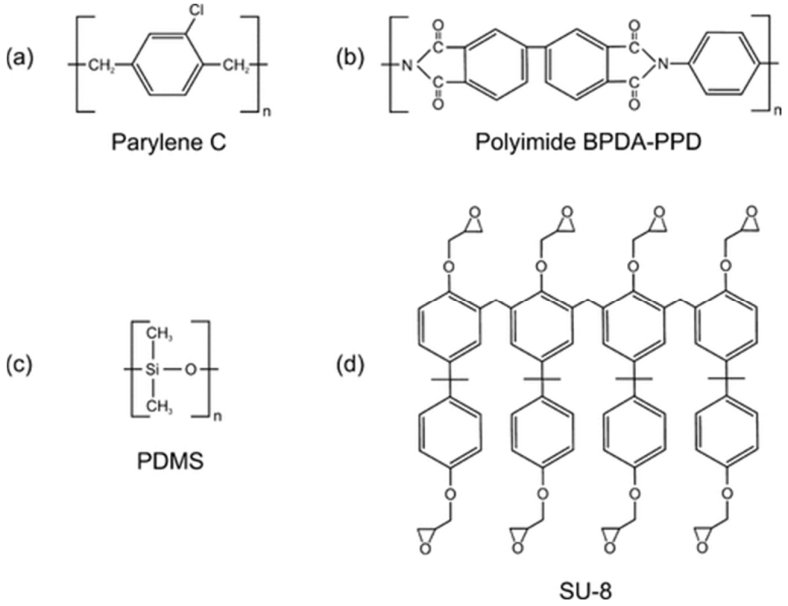

Figure 8. a) The monomer of Parylene C b) The structure of BPDA-PPD monomer. c) The siloxane backbone of PMDS. d) The SU-8 resin backbone used in the resist. The figure is reprinted and adapted from Hassler et.al. (2010) under CC BY 4.0.

Paper 1 delves deeper into properties of polymers shown in Figure 8 and its relevance for patterning with EBL, but here the properties are described in general.

2.1.1.1 Parylene

Parylene (polyparaxylylene) is a family of thermoplastic polymers, consisting of several variants with tailored properties, including Parylene C [poly(dichloro-p-xylylene)], the most prevalent in biomedical engineering[2]. The monomer of Parylene C is shown in Figure 8a. Renowned for its exceptional biological inertness, high dielectric strength, and chemical stability, Parylene C serves as both a flexible substrate and conformal encapsulation layer in neural implants and bioelectronic devices[13,72,73]. It is usually deposited using CVD to make very uniform, conforming layers[74].

Over the past decades, Parylene C has become a cornerstone in medical implants, including retinal prostheses, cochlear implants, and deep brain stimulators, where it provides robust hermetic sealing against moisture ingress while maintaining signal integrity and tissue biocompatibility[75,76]. Its minimal foreign body reaction ensures long-term stability, according to ISO 10993 standards and USP Class VI compliance[59].

2.1.1.2 Polyimide

PI is a polymer characterized by repeating imide groups (shown in Figure 8b), renowned for its exceptional thermal stability, mechanical robustness, chemical inertness, and superior electrical insulation[2]. These properties make it a preferred material in bioelectronics as it can withstand, e.g., heating during processing, mechanical stress during implantation, but at the same time being highly flexible and possess chemical inertness for long-term stability in the body[2,77]. Important is also the high dielectric strength and low humidity uptake, which makes it possible to generate exceptionally thin-films which possess reliable insulating properties over time[78].

PI has been employed as a substrate for medical devices over the past three decades, demonstrating mild FBR, and a high structural integrity[2]. Among various PI formulations, the BPDA/PPD (3,3′,4,4′-biphenyltetracarboxylic dianhydride/p-phenylenediamine) type that is commercially available as DuPont™ PI-2611 or UBE U-Varnish[2], is most prevalent in neural implants due to its excellent chemical resistance and low water uptake[12].

Although not formally FDA-approved, PI satisfies ISO 10993 biocompatibility standards and meets USP Class VI requirements[2,59]. In vivo studies confirm its safety, with implants showing no adverse tissue reactions over 32 weeks[59].

2.1.1.3 PMDS

Polydimethylsiloxane (PDMS), commonly known as silicone, is a synthetic organosilicon polymer with a flexible backbone of repeating siloxane bonds with methyl groups[2,79] (shown in Figure 8c). PDMS substrates provides high biocompatibility, flexibility, chemical inertness, low modulus, and a high resistance to biodegradation, making it a great material for long-term biomedical implants and soft electronics[2,80].

PDMS has been extensively utilized in medical devices for over five decades, particularly in neural interfaces such as cardiac pacemakers, cochlear implants, peripheral nerve stimulation cuffs and books, and central nervous system electrode arrays[2,59,80].

2.1.1.4 SU-8

SU-8 is a negative-tone, epoxy-based resist formulation consisting of a SU-8 epoxy oligomer (shown in Figure 8d), photoacid generator (PAG), and cyclopentanone solvent, renowned for providing pattern fidelity, high aspect-ratio structures, and robust mechanical properties after crosslinking[2,14]. These attributes make it versatile for micromachining, micro-optics, microfluidics, and MEMS packaging in electronics and photonics[81].

In biomedical engineering, SU-8 has been utilized as a substrate material for neural interfaces, including rigid shafts for penetrating CNS electrode arrays, sieve designs promoting axonal regeneration through microholes, waveguide cores for hybrid optogenetic stimulation, and integrated microfluidic channels for drug delivery[2,14]. Its biocompatibility, validated by ISO 10993 cytotoxicity assays and short-term in vitro studies, shows low inflammatory response[81].

2.1.1.5 LCP

Liquid crystal polymers (LCPs) are thermoplastic materials composed of rigid-rod and flexible-spacer monomers that self-align into ordered, crystalline-like domains under specific thermal conditions[82]. These thermotropic polymers show high thermal stability and chemical

resistance, low moisture absorption, and water vapor transmission rates, surpassing PI and PDMS in hermeticity[2,82].

LCPs have been established in high-reliability electronics, including high-density flexible PCBs, microwave circuits, and semiconductor packaging[2]. In the biomedical field LCPs has many promising attributes, but they still lack data in chronic in vivo studies[2]. However, their dimensional stability, biocompatibility (ISO 10993 compliant), and barrier properties position LCPs as suitable encapsulation materials for long-term implants, with emerging in vivo studies demonstrating reduced delamination and foreign body response compared to conventional polymers[82].

2.1.2 Electrode materials

Because the charge injection capacity of the noble metals is not enough for neural recording, there is a need for electrode materials that has a low impedance and high charge injection capacity[83]. IrOx is a useful electrode material for neural implant due to its extraordinary electrochemical properties and low impedance. Apart from that, it is also corrosion resistant, non-toxic to cells and exhibits higher CIC than any other known electrode material[84]. In fact, IrOx has a 30-fold higher CIC compared to Pt[79]. It is commonly deposited electrochemically by cycling an iridium (Ir) metal electrode between positive and negative potential in an aqueous electrolyte or PBS at pH 7, or deposited through reactive DC magnetron sputtering (described more in Section 2.2.2.2) from an Ir target[85]. In this case it's called sputtered iridium oxide film, SIROF. This is usually performed in an argon-oxygen plasma or humidified oxygen discharge[53]. The sputter-deposited IrOx films yield very porous and high-surface area structures, as shown in Figure 9a-c.

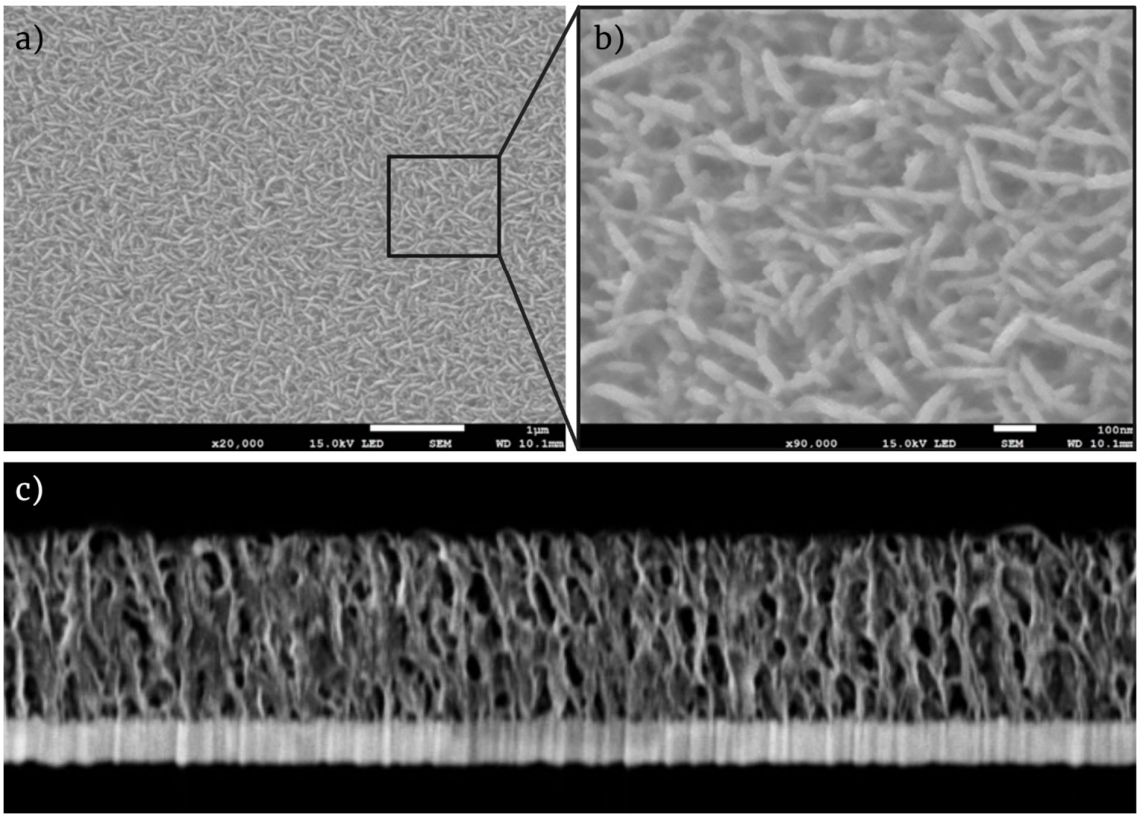

Figure 9. a) The porous SIROF structure from above. Picture credits: Lukas Matter. b) Zoom in of the SIROF structure. Picture credits: Lukas Matter. c) The cross section showing the porosity of the SIROF layer. Picture credits: Paul Cvancara and Yara Baslan.

The hydrated IrOx film, also called activated iridium oxide film (AIROF), is formed by electrochemical cycling or pulsing the iridium metal electrodes in aqueous electrolyte[84]. The activation is performed to increase the charge storage capacity (CSC) and charge injection capacity (CIC) to optimize it for neural stimulation. During stimulation or recording, the charge is injected or extracted through reversible reduction and oxidation of Ir^{3+}/Ir^{4+} valence states[53].

2.1.3 Conducting material

For neural devices, the conducting material must have high conductivity, low and stable impedance, long-term chemical stability in saline and strong adhesion to the substrate. Noble metals are mostly used because they combine excellent electrical conductivity with corrosion resistance, chemical inertness, and good biocompatibility, critical characteristics for implants[59].

Au offers superior conductivity with a bulk resistivity of approximately 2.44 μΩ·cm, outperforming Pt's approximately 10.6 μΩ·cm[86]. Platinum compensates with higher charge

injection capacity when electroplated or textured (e.g., platinum black), making it preferable for stimulation electrodes requiring safe, high-current delivery without Faradaic reactions[87].

Metal adhesion to the substrate is critical for the structural integrity and long-term functionality of microfabricated neural implants, as delamination can severely compromise thin-film electrodes, particularly during chronic implantation[12]. Poor adhesion during fabrication typically originates from weak van der Waals bonding, thermal expansion mismatch, or surface contamination, for example, residual photoresist underneath the deposited metal after development in a lift-off process[12,88]. In implanted devices, the metal-PI interface can further fail due to moisture penetration, chemical degradation arising from inflammatory reactions, and electrical loads induced by electrochemical stimulation[12]. The adhesion challenges can be mitigated by thin adhesion layers such as chromium (Cr) or titanium (Ti), silicon carbide, silane coupling agents, and oxygen plasma treatment[12]. Cr and Ti form carbide-like bonds to the PI surface, thereby enhancing adhesion[12]. However, while Cr has been shown to be a more effective adhesion promoter than Ti, Cr also has a significant disadvantage as its toxic ions may damage surrounding tissue if they leak out[12].

Adhesion is also influenced by the deposition method, for example the adhesion can be improved by sputtering the metallization layer instead of evaporation, as the higher-energy sputtered particles yield higher packing densities and better surface coverage[12]. This aspect is further discussed in Section 2.2.2.

2.2 Micro- and nanofabrication methods

Micro- and nanofabrication, together with thin-film technology, constitute the foundation of microsystems engineering. These techniques enable the realization of highly precise structures at micro- and nanometer scales, which are essential for applications such as neural implants. By combining deposition, patterning, and etching processes, functional devices are constructed layer by layer on substrates including silicon and polymer-based materials[89,90]. Some typical micro- and nanofabrication processes includes[90–93]:

- Lithography: Photolithography or electron-beam lithography (EBL)
- Material deposition techniques: Physical vapor deposition (PVD) techniques such as evaporation or sputtering to deposit, e.g., metal films.

- Etching: Wet (chemical etching) or dry (e.g. reactive ion etching) removes material selectively.

2.2.1 Lithography

Lithography is a fundamental pattern-transfer methodology in microfabrication. The wafer is coated with a resist, which is a temporary, pattern-forming coating used in lithography to transfer a design onto a substrate[90]. The resist changes its solubility after exposure, so that parts of it can be removed by dissolving parts of the resist, i.e. developing to create the desired pattern and acts as a mask for later steps such as etching, deposition, or lift-off. The resist can be either positive or negative; for a positive resist, the exposed region is removed by dissolving the molecules in the developer while for a negative resist, the unexposed region is removed by the developer[90]. The goal for lithography is that the pattern features are well-defined and have an accurate feature size.

2.2.1.1 Optical lithography

Optical lithography is a patterning method that uses light to transfer a design from a mask onto a light-sensitive resist on a substrate, usually a silicon wafer[94]. Photolithography can be performed with a mask aligner, in which light is illuminated through a photomask with the designed pattern, with transparent sections where the UV light goes through and opaque section where the light will be blocked, precisely transferring the pattern to the substrate[92,94]. A typical mask aligner photolithography which uses a Hg source that illuminates at 436 and 365 nm[95] one can theoretically attain a resolution down to sub 0.8 µm[96], but reproducible feature of 1.5-3 µm is more typical. Furthermore, in research settings, this method is limited by the manual alignment which is about 0.5 µm but it also depends on the skills of the operator. To fabricate smaller features using mask photolithography, deep UV and extreme UV are used[97,98]. Using mask lithography is by far the lithographic method with the highest throughput and therefore it's used for mass production of micro- and nanocomponent[99].

Optical lithography can also be performed using a laser source in a technique known as laser lithography[100]. This direct-write method uses a focused laser beam to transfer patterns onto the substrate without the need for a photomask. Compared to conventional mask aligner lithography, laser lithography offers lower throughput but provides greater flexibility in design and allows for virtually unlimited design iterations[99].

Another commonly employed direct writing technique is the maskless aligner which uses a programmable spatial light modulator, typically a digital micromirror device with 1-2 million independently addressable mirrors functioning as a digital photomask[101]. The entire array then illuminates simultaneously, making it much faster compared to conventional direct writing lithography[101]. Laser lithography with a maskless aligner, however, doesn't provide as high resolution and overlay conventional direct writing lithography, but is a great tool for prototyping with resolution of >1.5 um[101,102].

Each optical lithographic process in this work is performed with MLA, due to high flexibility offered using this method.

2.2.1.2 E-beam lithography

EBL is a maskless nanofabrication technique that uses a focused beam of high-energy electrons (typically 10-100 keV) from a field-emission gun, directed by electromagnetic lenses and deflection coils, to pattern custom nanoscale features directly onto a substrate coated with an electron-sensitive resist[93,103]. Due to the short de Broglie wavelength of electrons, but is constrained by the scattering nature of electrons, aberrations, and proximity effects, yielding features down to 7-10 nm[92,93,103].

EBL is, similarly to laser lithographic systems, a direct writing tool, commonly employed for prototyping nano-scale features. However, it's inherently slow due to the scanning operation causing low throughput, especially for larger wafers or more complex patterns, and is thus more commonly employed in research settings compared to mass production[93,103].

EBL is described more in debt in Paper A.

2.2.2 Thin-film deposition

Thin-film deposition are methods for creating layers of material, with a thickness range of nm to µm thick onto specific substrates to fabricate micro and nanocomponents. These methods are divided into groups depending on their mechanism; physical methods (physical vapor deposition, PVD: sputtering and evaporation) that eject atoms mechanically from the target and chemical methods (CVD and atomic layer deposition, ALD) that use reactions to create the layer[90]. This section will be focused on PVD as this is most relevant for this thesis.

2.2.2.1 *Evaporation*

Evaporation is a thin-film deposition technique where a solid material is heated in vacuum until it vaporizes and then is condensed as a thin film on a cooler substrate[90,104]. The source is heated either thermally or by using an ion or electron beam[90,105]. During evaporation, the atoms travel from the heated source, in straight lines due to long mean free paths which is minimizing gas collisions[90]. Because of the increased directionality with this deposition method, there is often poor step coverage on the sidewalls (illustrated in Figure 10a) which makes evaporation particularly suitable for lift-off[104]. Compared to sputtering, the film is less dense and the adhesion of the material to the substrate is worse, although the purity of the evaporated film tend to be higher compared to sputtered films[90]. Metals are commonly evaporated materials.

In this work, the metallization layer is deposited through evaporation unless its IrOx or else stated.

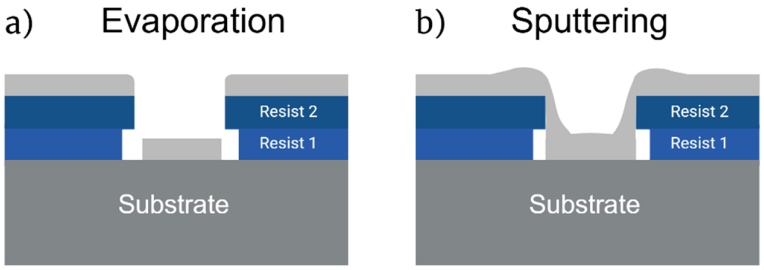

Figure 10. a) Cross section of a sample with patterned bilayer resists and an evaporated metal layer. The deposited metal (light gray) layer in direct contact with the substrate and on top of the resist does not merge due to the high directionality when evaporating the metal film. b) The profile of a sputtered metal film. The metal layer on the substrate might merge with the metal layer on top of the resists causing a troublesome lift-off.

2.2.2.2 *Sputtering*

Sputtering, in contrast, is a physical vapor deposition (PVD) technique wherein a target material is ejected from a cathode source via momentum transfer from ionized inert gas ions (typically argon ions, Ar^+), enabling conformal thin-film deposition[104]. Sputtering produces dense, adherent films with a high step coverage (shown in Figure 10b), making it indispensable for metallizing high-aspect-ratio features, but it can on the other hand be difficult for lift-off

processes[90]. This method also yields superior film quality with low defect density, controlled stoichiometry, and improved adhesion to the substrate[90].

2.2.3 Etching

Etching in micro- and nanofabrication, refers broadly to the selective removal of material from a substrate or thin film to transfer a pattern defined by a mask[90]. The mask can be resist or metal (hard mask) and it protects certain regions, while the etchant attacks only the exposed areas, thereby shaping the underlying layer into the desired features such as lines, electrodes, or trenches. A good etch mask must adhere well to the surface, withstand etch chemistry, and preserve feature dimensions throughout the process, without leaving deposits on the sample.

When etching with a resist mask, the resist is spin-coated on the wafer, baked and rehydrated before being exposed and subsequently developed. The unprotected polymer underneath the mask is then etched using RIE and after the etching process finishes, the remaining resist on the unetched areas is removed. The process is illustrated in Figure 11a.

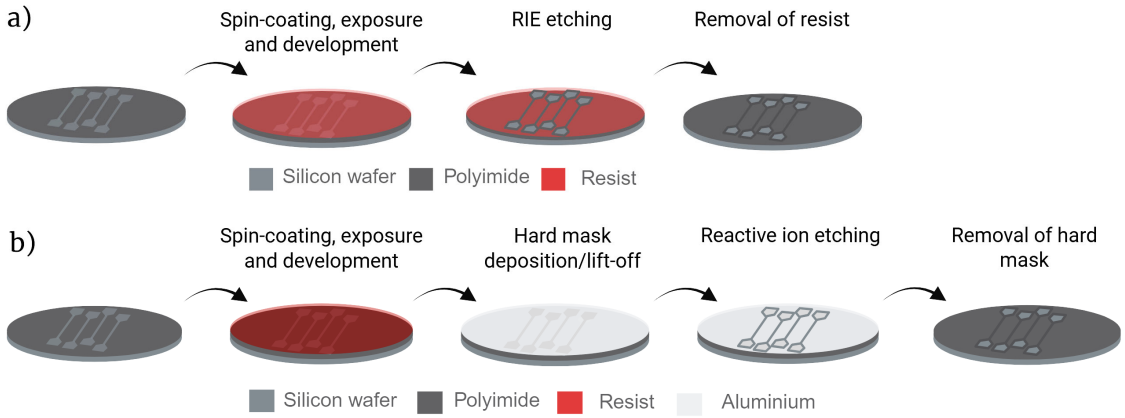

Figure 11. a) The process of etching with a resist mask. b) The process of etching with a hard mask.

During polymer etching, the selectivity between the polymer and the resist mask determines the extent to which the mask is preserved during pattern transfer; a high selectivity is required to maintain feature fidelity and achieve sufficient etch depth[106,107]. Due to low selectivity of the resist mask when etching polymers, the resist needs to be thick enough to protect the wafer during the whole etching process[106], which substantially restrict achievable resolution.

A hard mask is more durable and can be used when the resist itself will not survive the etching process, and thus also offers higher selectivity[107]. In addition, a hard mask improves pattern fidelity, etch depth, and process robustness, at the cost of adding one extra deposition and pattern-transfer step. Common hard mask material is inorganic material such as silicon oxide, silicon nitride, Al oxide or metals such as Cr and aluminium (Al)[108–110]. The hard mask can be patterned using lift off, a process that starts with spin-coating, exposing and developing. The metal is subsequently deposited on top of the wafer, and the excessive metal is removed through lift-off. The process is illustrated in Figure 11b.

Etching can be isotropic or anisotropic; for isotropic etching the material is removed uniformly in all directions, creating rounded profiles, while in anisotropic etching the material is removed faster in a specific direction, producing sharper, high-aspect-ratio structures with vertical sidewalls[91].

Etching processes are divided into two main categories: wet etching and dry (plasma-based) etching, described in this chapter[90,91]

2.2.3.1 Dry etching

Dry etching is plasma-based microfabrication process that removes material from a substrate surface without using liquid chemicals. Plasma generates reactive ions and radicals through radiofrequency or ICP power that bombards the surface, combining chemical reactions with physical sputtering to remove the material[90,91]. Etching can be performed by pure plasma etching, where chemical reactions dominates the etching, by physical sputtering, where the material is simply sputtered away or by reactive ion etching that combines sputtering with chemical reaction from reactive gases[90,107].

Compared with wet etching, dry etching generally offers better control over critical dimensions, reduced undercutting, and compatibility with high-aspect-ratio structures[91]. Parameters such as gas composition, pressure, power, and bias voltage are tuned to balance etch rate, selectivity to the mask, and sidewall profile for a given process[107].

Physical sputtering in dry etching is a purely physical removal process where high-energy ions (typically Ar^+) bombard a substrate surface, dislodging atoms through direct momentum transfer without chemical reactions[90] (illustrated in Figure 12a). This etching technique is widely used in microfabrication, offering anisotropic etching and is generally material independent, allowing for etching highly unreactive materials such as Pt[90,111].

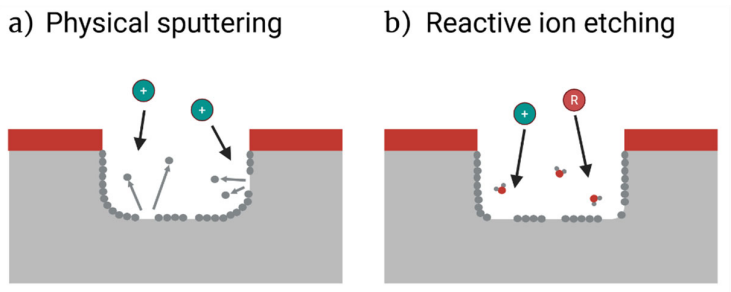

Figure 12. a) The mechanism of physical sputtering, using high-energy ions that physically removes the material. b) The mechanism of plasma etching using reactive species to remove materials through chemical reactions. c) The mechanisms of RIE which use both chemical reaction from the radicals and physical milling from ions.

Reactive ion etching (RIE) combines chemical reactions from reactive plasma species with physical ion bombardment to achieve highly anisotropic material removal (shown in Figure 12b). Because it uses chemical reaction to remove the material, it is more material dependent compared to physical sputtering[107]. RIE occurs in a vacuum chamber where reactive gases are introduced and ionized into plasma by RF electromagnetic fields[90]. The substrate is placed on a negative biased electrode, accelerating positive ions toward substrate surface to enhance etching rates and remove byproducts via sputtering[90].

Another type of RIE etching is by using inductively coupled plasma (ICP-RIE). ICP-RIE separates plasma generation from substrate biasing using an inductive coil to sustain high-density plasma via inductive coupling, independent of the substrate RF chuck[112]. This enables high etch rates at low pressures with precise control over ion energy, minimizing plasma-induced damage and provide etched structures with high anisotropy[107].

In this work RIE is used to descum (remove residual resist after development) the surface after lithography process step and improve adhesion the metal-PI bonding as well as PI-PI bonding. ICP-RIE is used to etch PI to open the outlines of the structures, pads and electrodes.

2.2.3.2 Wet etching

Wet etching uses a liquid chemical solution, or etchant, that selectively removes the material from a substrate surface[90]. In micro- and nanofabrication, wet etching is widely used for its simplicity, high etch rate, and good material selectivity, although it tends to be isotropic and can cause undercutting of features[90]. Common applications include patterning metals, such as Al and copper, oxides, and semiconductors such as silicon, or glass. The etch rate and anisotropy depend strongly on the etchant composition, concentration, temperature, and substrate crystal orientation.

In this work, wet etching is used to remove the Al hard mask.

2.2.4 Pattern transfer

Structuring metal features can be performed either through lift-off or etching. Lift-off is an additive microfabrication technique used to pattern thin films. The lift-off process involves depositing the material layer to be patterned after photoresist spin-coating and patterning, followed by selective removal of the resist in solvent, lifting away the overlying material from undesired regions, leaving behind well-defined structures on the substrate[90]. A typical lift-off process on polymeric material is illustrated in Figure 13. Lift-off generally provides clean, high-fidelity patterns, making it particularly suitable for metals that would otherwise necessitate aggressive wet or dry etchants capable of damaging underlying layer. Moreover, lift-off exhibits reduced dependence on material-specific etch chemistries compared to subtractive etching methods, facilitating process standardization across diverse metallization schemes. Pt and Au, common metallization materials in bioelectronic implants are notably chemically inert and thus preferentially patterned via lift-off.

Etching is described more in depth under Section 2.2.3, but here it is outlined more in terms of a patterning technique. Etching is a subtractive patterning approach for which the material is selectively removed from exposed regions following resist exposure and development, utilizing either wet chemical solutions or plasma to define device features[94]. This method is suitable for high throughput production of precise geometries, particularly for dielectrics and refractory metals not suitable for lift-off. However, etching often demands material-specific recipes, reactive ion etching (RIE) with can be challenging for noble metals, often used in bioelectronics. However, to improve adhesion and fidelity of small structures of the

metallization layer to the PI, sputtering of the Pt and then etching can be an alternative to lift-off.

The process steps of lift-off and etching is shown in Figure 13.

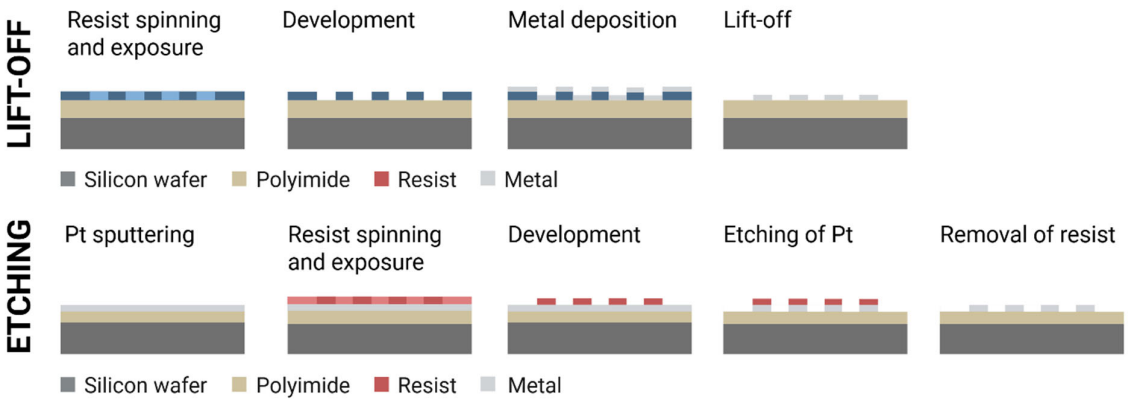

Figure 13. Process flows of lift-off and etching. With lift-off, the wafer is spin-coated with the resist and subsequently exposed and developed. The Pt is then deposited preferably with evaporation, and the unpatterned metal is lastly lifted off. When using etching for shaping the metal features, the Pt is first deposited by sputtering, and the resist is spin-coated, exposed and developed subsequently. The Pt is the etched using Ar plasma and the resist is lastly removed.

2.3 Analytical methods

2.3.1 SEM

Scanning electron microscopy (SEM) provides high-resolution surface imaging essential for characterizing sub-micron structures and features, revealing topography, defects, and thin-film integrity down to a few nm[113]. During operation, a finely focused electron beam raster-scans the sample, generating secondary electrons for topography, backscattered electrons for compositional contrast, and X-rays for elemental analysis via energy-dispersive X-ray spectroscopy. The electrons are detected using an electron detector and an image is then built from the surface.

In this thesis, SEM has been used to analyze the fabricated micro- and nanostructures. Prior to the SEM analysis, a conducting polymer film, E-spacer, was spin-coated on the wafers to provide mitigation of charge build up during SEM analysis.

Optical microscopy and optical profilometer were used as a complement to SEM for analysis larger structures and providing 3D scanning of layered devices.

2.3.2 XPS

X-ray photoelectron spectroscopy (XPS), enables non-destructive surface chemical analysis with very high sensitivity, probing the top of the sample (approximately 5 nm[114]) by irradiating the sample with X-rays and detect the photoelectrons from the material's surface[115]. From the kinetic energy of the photoelectrons and number of electrons ejected from the surface, the elements can be deduced together with the chemical state, electronic structure and density of the electronic states in the material. By sputter-etching, information about the sample can be detected deeper into the sample, making this method highly versatile.

In this work, XPS was used to detect Al residues after removal of the hard mask. The survey spectra were acquired using a monochromatic Al Kα source under high vacuum.

2.3.3 Electrochemical validation

2.3.3.1 Cyclic voltammetry

Employing a three-electrode setup, CV linearly scans the potential, typically in a triangular waveform at controlled scan rates, measuring the current response that yields a characteristic voltammogram with anodic and cathodic peaks (shown in Figure 14a) giving the current ratios to diagnose reversibility and kinetics[116]. For bioelectronic device characterization, CV quantifies effective surface area, CSC and coating stability under physiological conditions[117].

In this work, CV has been mainly performed to activate IrOx electrodes (as described in Section 2.1.2.1), to confirm functionality of electrodes and to "clean" the surface by performing a couple of cyclic scans of the electrodes prior to electrochemical impedance spectroscopy (EIS). The CV is performed between 0.9 V and -0.6 V with a scan rate of 0.1 V/s.

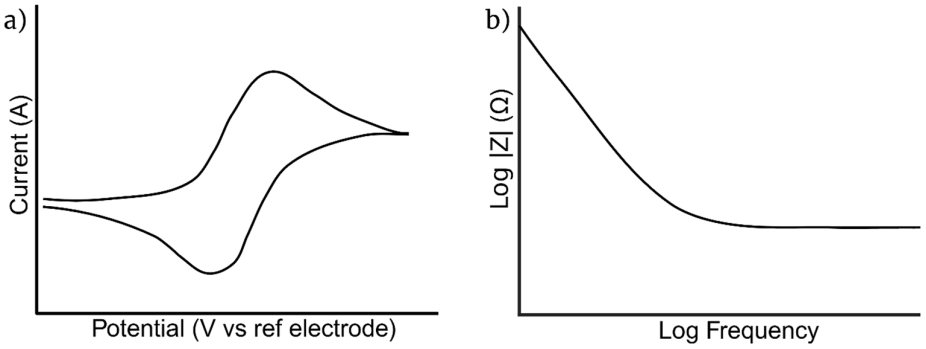

Figure 14. a) An example of a cyclic voltammogram. b) A Bode plot which is a typical representation of electrochemical impedance spectroscopy data

2.3.3.2 Electrochemical impedance spectroscopy

EIS is a non-destructive electroanalytical methodology that elucidates the dynamic interfacial processes within electrochemical systems[46,118]. By superimposing a small-amplitude sinusoidal voltage perturbation across a broad frequency spectrum, typically spanning millihertz to megahertz regimes, EIS quantifies the resultant current response, yielding the complex impedance $Z(\omega) = Z' + jZ''$, where Z' and Z'' denote the real and imaginary components[118].

EIS explores the frequency-dependent electrochemical behavior of interfaces, including reaction kinetics and mechanisms, mass transport properties and system resistances and capacitance[118]. Data are usually visualized via Nyquist- and Bode plots (shown in Figure 14b), facilitating regression to equivalent circuit models that parameterize these elements.

In the context of neural interface microdevices, low electrode impedance is critical for recorded signal quality and the 1 kHz impedance point is often used as benchmark for electrodes that record neural spikes[119]. Furthermore, EIS is useful for monitoring long-term stability of the recording electrodes under physiological conditions, and can even be applied to monitor implants in vivo [9,46,120].

EIS was used in this work to compare the impedance of interconnects and electrodes with varying dimensions and areas over a frequency range of 0.1 Hz to $1 \cdot 10^5$ Hz, using a 0.1 V sine-wave perturbation and 4 frequencies per decade. The test structure that was used to assess the impedance dependence line width variations is shown in Figure 15.

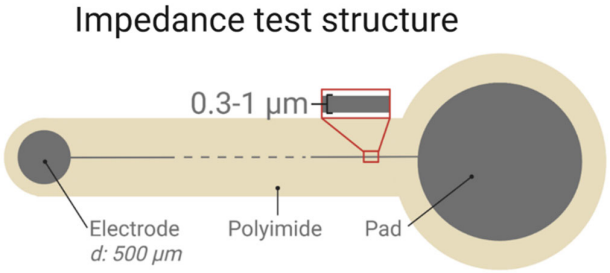

Figure 15. A test structure to assess impedance of varying electrode material or line width dimensions.

2.3.4 Electrical validation

2.3.4.1 Resistivity and resistance measurements

Resistance (R) is the opposition to current flow within an object, and it is defined in Equation 1, also known as Ohm's law, wherein V is the potential and I is the current, and is measured in ohms (Ω)[118,121].

$$R = \frac{V}{I} \tag{1}$$

Resistance depends on the material and the geometry of the object, such as its length and cross-sectional area. Resistivity, on the other hand, is an intrinsic material property that describes how strongly a material resists current flow, independent of shape or size[121]. For a uniform conductor, the resistance and resistivity as shown in Equation 2, where ρ is resistivity, L is length, and A is cross-sectional area[121].

$$R = \frac{\rho L}{A} \tag{2}$$

Conductivity is the inverse of resistivity, and determines how conductive the material is[121].

Sheet resistance is the electrical resistance of a thin, uniform film, defined as the resistance between opposite edges of a square piece of that film. It is expressed in ohms per square (Ω/□) and depends only on the material's resistivity and the film thickness, not on the size of the square. For a film of resistivity ρ and thickness t, the sheet resistance is given by Equation 3.

$$R_s = \rho/t \tag{3}$$

This 2D resistance concept is widely used in microelectronics and thin-film devices, because it directly relates to the resistance of any rectangular conductor made from that film. Sheet resistance is commonly measured using a four-point probe to avoid errors from contact resistance.

Two-point probe (2PP) measurement is a straightforward technique for determining electrical resistance by measuring the voltage drop and current through a sample using the same two contacts[122]. A 2PP test structure used in this thesis is shown in Figure 16, and the resistance measurements are conducted by applying potential sweep between -5 and 5 V with a step size of 0.1 V and measure the current response for which the resistance is calculated and averaged.

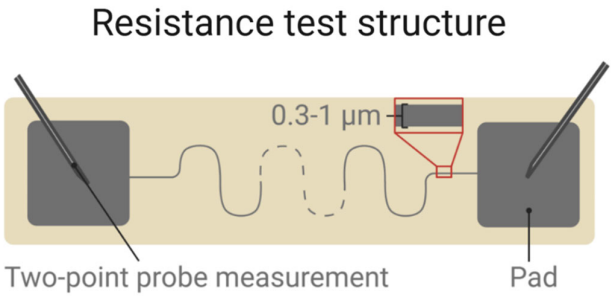

Figure 16. A test structure to assess resistance with 2PP measurements.

Although simple and widely used, the method is influenced by lead and contact resistances, which can reduce accuracy when characterizing a material with this method. To eliminate the effect of contact resistance, four-point probe (4PP) measurement is instead used to determine resistivity or sheet resistance by passing current through two outer probes and measuring the voltage across two inner probes[122]. The principal difference between 2PP and 4PP measurements are shown in Figure 17a and 17b.

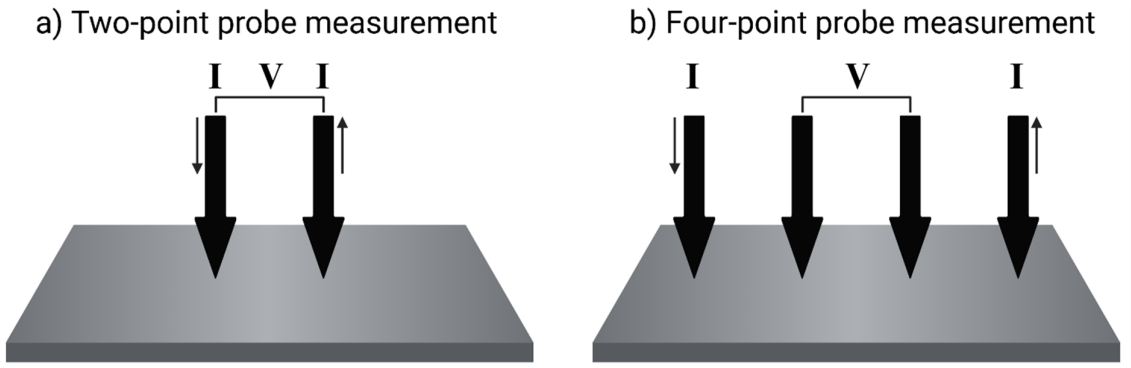

Figure 17. a) Schematic showing how two-point probe measurements are performed. The current is forced between two probes, and the same probes are used to measure the voltage drop. b) Schematic of four-point probe measurement. The current is forced between two outer probes, and the voltage drop is measured between two inner probes. This way, the impact of contact resistance is eliminated.

A common structure for measuring sheet resistance using the 4PP measurement method is shown in Figure 18.

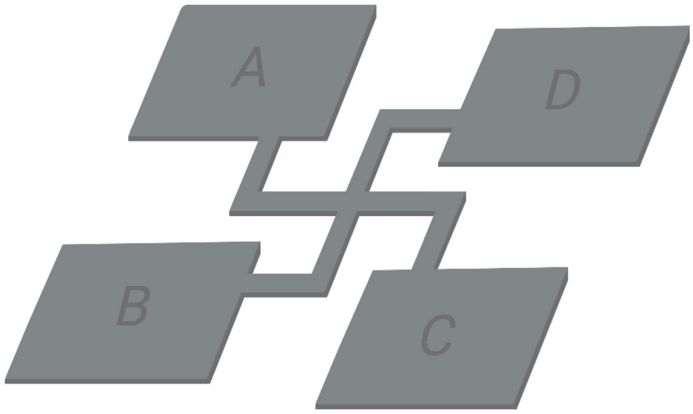

Figure 18. The cross structure used to assess sheet resistance.

The sheet resistance is measured from the cross section of the structures, at 0°, by forcing a current between terminal A and D and measure the voltage drop between terminals B and C[123]. The current is then reversed, so that the current is forced between terminal D and A and the voltage drop is measured between C and B. This is followed by measuring the resistance at 90° between terminal A and B, by forcing a current and measuring the voltage drop between terminals C and D and again reversing the current. The four resistance values gathered from the measurements are average as shown in Equation 4.

$$R(\pm I) = \frac{R_0(\pm I) + R_{90}(\pm I)}{2} \tag{4}$$

The sheet resistance (Rs) is calculated from the resulting resistance (R) as shown in Equation 5.

$$R_S = \frac{\pi R}{ln\,(2)} \tag{5}$$

By using resistance measurements, the width and pitch of single and double lines can be assessed though electrical measurements on test structures: the bridge and split-bridge structure[123] (shown in Figure 22a and 22b, respectively).

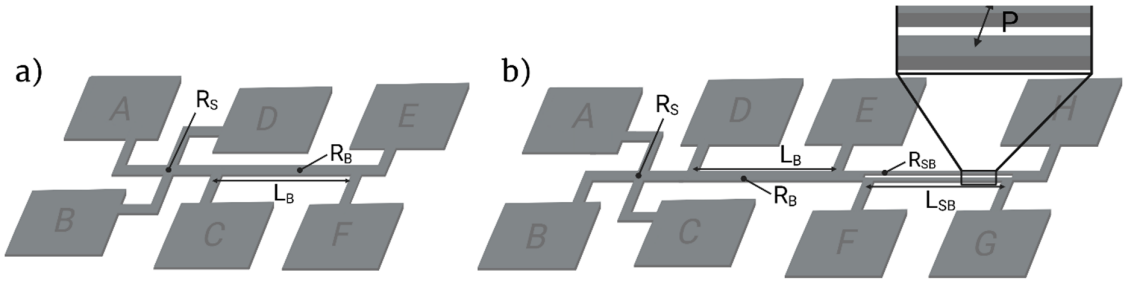

Figure 19. a) Schematic of the bridge structure. The sheet resistance assessed from the cross section of the structure is denoted R_S and bridge resistance is denoted R_B. The length of the bridge (L_B) is 300 µm. b) Schematic of the split-bridge structure. The sheet resistance is denoted R_S, bridge resistance R_B and split-bridge resistance R_{SP}.

With a series of four-point probe measurements, the electrical width of the single line in the bridge structure and the pitch of the double line in the split-bridge structure are calculated. The sheet resistance of the cross structure in the bridge and split-bridge structure is measured the same way as the cross structure shown in Figure 18. The resistance of the bridge is measured by forcing a current between pad A and pad E, measuring the voltage drop between pad C and F, giving the resistance R_b[123]. The measurement is then reversed, and the resistance is averaged. The electrical width of the bridge is then calculated as shown in Equation 6.

$$W_b = \frac{R_S L_b}{R_b} \tag{6}$$

The pitch of the split-bridge microstructures is determined by first measuring and calculating the sheet resistance and electrical width of the single line of the structure, in the same manner as for the bridge structure[123]. The electrical width of the split bridge is given by Equation 7.

$$W_B = 2W + S \tag{7}$$

And the width of the two conducting lines is given by Equation 8.

$$W_S = 2W \tag{8}$$

The resistance of the split-bridge (R_{SB}) is calculated by averaging the measured resistance, from both directions, and the electrical width (W_{SB}) of the conducting lines is calculated as shown in Equation 9.

$$W_{SP} = \frac{R_S L_S}{R_{SB}} \quad (9)$$

The spacing (S) between the conducting lines is calculated by subtracting the width of the split bridge from the width of the bridge, as presented in Equation 10.

$$S = W_B - W_{SP} \quad (10)$$

And pitch is calculated from Equation 11.

$$P = W + S \quad (11)$$

2.3.4.2 Crosstalk

Crosstalk refers to unintended coupling between neighboring signal lines, and it degrades signal integrity by introducing noise and distorting the desired signal[124]. For neural devices or bioelectronics, crosstalk is important especially for miniaturized devices, as tightly spaced interconnects, especially for thinner insulating material in between the lines, can pick up signals from one another, reducing recording specificity and potentially complicating data interpretation.

Crosstalk is measured by quantifying unwanted signal coupling between parallel lines (as shown in Figure 20), using an oscilloscope or vector network analyzer[124].

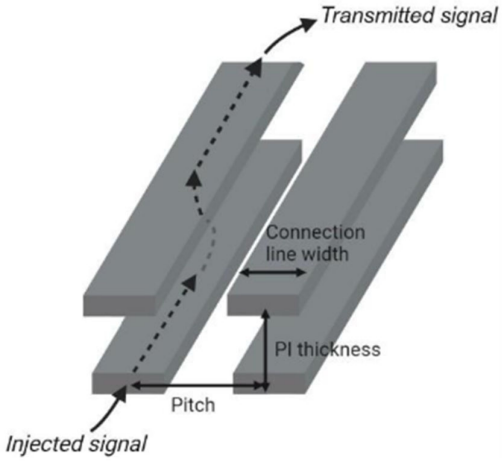

Figure 20. Schematic showing layered interconnects. Crosstalk is measured by injecting a signal into one line and the transmitted signal in adjacent line is quantified.

Crosstalk between adjacent lines can be resistive or capacitive[124]. Resistive coupling refers to physical contact between two lines and is independent of frequency. Capacitive coupling originates from displacement currents generated by time-varying potentials along the interconnect and is, contrary to resistive coupling, frequency-dependent, meaning the higher frequency, the more crosstalk.

3 Results

3.1 Miniaturization of implant features

Miniaturization of interconnects increases routing density within a given area, enabling higher electrode count. This improves the contact with individual fascicles in the nerve and can enhance both signal-to-noise ratio and signal selectivity. EBL was implemented on PI substrates as described in Paper A. The cross, bridge and split-bridge test structures were employed for measuring and calculating the width of single lines and pitch of double lines, as described in Section 2.3.4.1. The fabricated structures are shown in Figure 21a-c and the measurements are presented in Paper A. The resistance was measured by sweeping a current between 0 V and 1 V and measuring the resulting voltage drop.

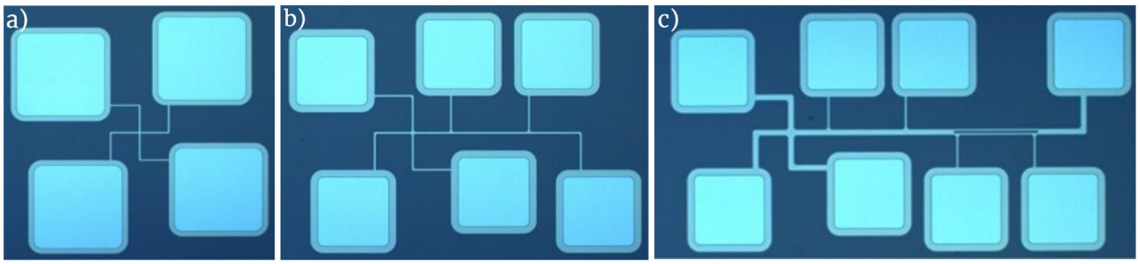

Figure 21. a) Fabricated cross structure for sheet resistance measurement. B) Fabricated bridge structure for measuring and calculating electrical width. c) Fabricated split-bridge structure for measuring and calculating electrical pitch.

With the lift-off process described in Paper A, structures down to 100 nm with and 200 nm pitch were fabricated, as shown in Figure 22a. A dense array with a higher number of sub-micrometer lines were also fabricated, shown in Figure 22b, with a line width down to 300 nm and pitch 600 nm, to represent the interconnects in a fabricated device.

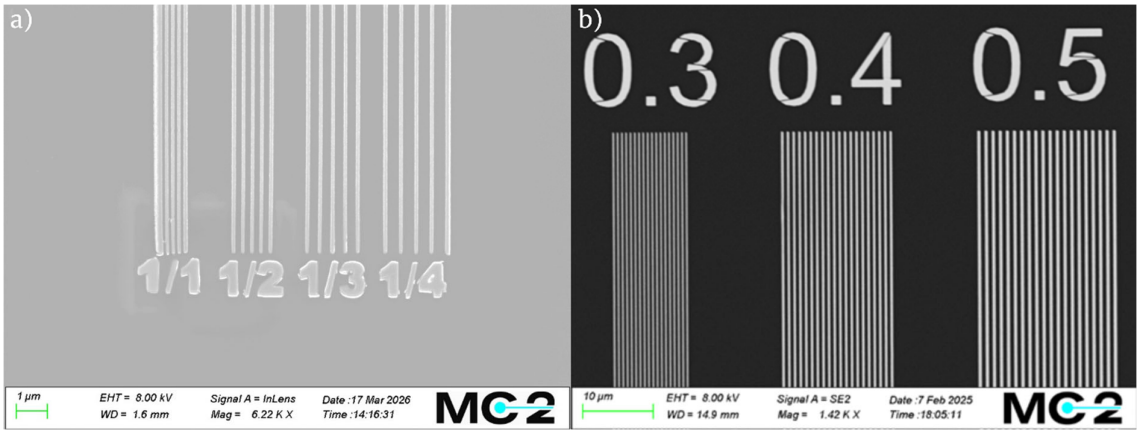

Figure 22. a) Fabricated features down to 100 nm width and 300 nm pitch. b) Dense array of lines with a line width of 300 nm and pitch 600 nm.

To explore how the dimension of the electrodes and interconnect influence the function of the devices, TIME devices were fabricated with circular and square electrode shape, with a diameter of 20 µm or 50 µm, with various line width. The design of the devices is shown in Figure 23a-b. Similarly to the bent design shown in Figure 6, the design is folded at the center and thus has two EA sites, arms and connector site.

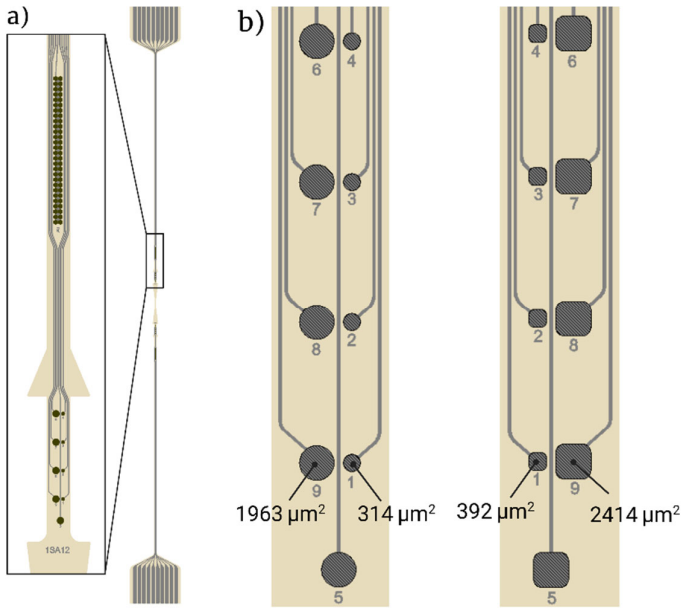

Figure 23. a) The design of the test devices, with a straight shape. b) The EA site of the two arms, having circular and square shaped electrodes with varying surface area.

To increase the number of electrodes on the EA site of the implant, minimizing the electrode diameter is essential. However, reducing the diameter causes an increase in impedance, which can ultimately limit the ability to inject stimulation pulses into the tissue. Here, electrode materials such as IrOx are essential as they can counteract the impedance increase with its superior electrochemical properties.

From a geometrical perspective, square-shaped electrodes provide a larger surface area than circular electrodes of the same width, as illustrated in Figure 23b. The circular electrode of 20 µm in diameter has a surface area of 314 μm^2, whereas the larger electrode (50 μm^2) has a surface area of 1963 μm^2. The square shaped electrode of 20×20 μm^2 has a surface area of 392 μm^2 and the larger (50×50 μm^2) has a surface area of 2414 μm^2. It should also be noted that this is only the calculated surface area from the design, and not the surface area after SIROF deposition, which is, of course, much larger due to the high porosity of IrOx.

Figure 24a shows the measured impedance of square and circular electrodes with varying diameters. The results indicate a slight difference in impedance between the two geometries, despite the increased surface area of the square electrodes. Thus, square-shaped electrodes enable more efficient use of the available space on the EA.

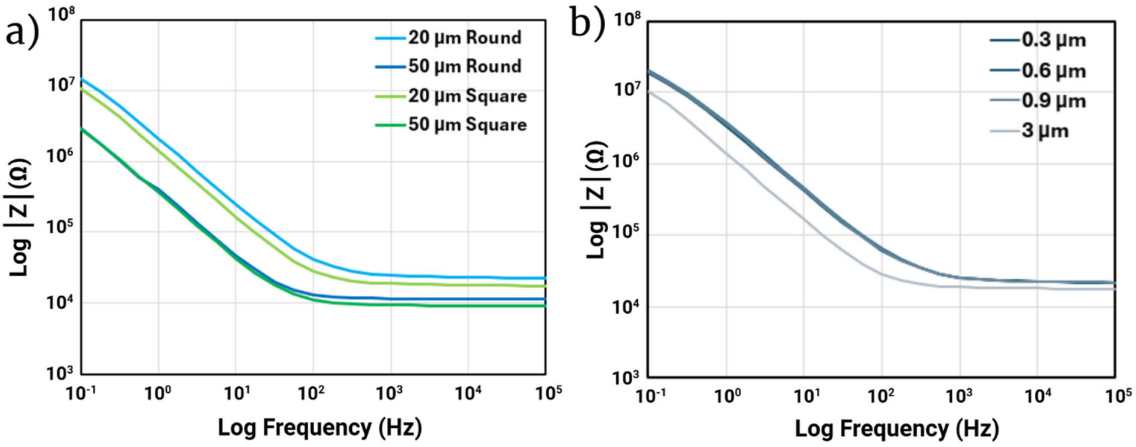

Figure 24. a) The measured impedance of electrodes connected with interconnects of line widths varying between 0.3-0.9 µm. b) The measured impedance of circular and square shape electrodes of 20 µm or 50 µm in diameter.

In addition, the impedance contribution from the interconnects increases as their dimensions are reduced, further emphasizing the need for low electrode impedance to ensure effective pulse delivery. Figure 24b presents the measured impedance for IrOx electrodes with a diameter of

20 µm, with Pt interconnects of line widths of 0.3-0.9 µm as well as 3 µm. It should be added that the sub-micrometer lie width is only on the EA site, and not the arms, and thus reach a maximum length of approximately 1 mm. The graph demonstrates that there is not a large difference between the sub-micrometer interconnects, and at 1 kHz frequency, there is only a small difference in the impedance between the sub-micrometer interconnects and the 3 µm interconnect.

3.2 Material selection for miniaturized devices

As interconnect widths go from the micrometer to the sub-micrometer regime, the high conductivity of the interconnect material becomes essential to ensure proper signal transmission. The increase in resistance is more pronounced at smaller dimensions due to enhanced surface and grain-boundary scattering in thin-film conductors.

As described in Section 2.1.3, Pt and Au are among the most used materials in bioelectronic devices. Here the conductance of a 100-nm-thick Au film with that of Pt films that is 100–300 nm thick is compared (Figure 25a), using the bridge structure shown in Figure 19a (Section 2.3.4.1). Conductance increases linearly with increasing line width. To achieve high-resolution structures with EBL, the resist must be kept thin, which in turn limits the maximum metallization thickness that can be used. By employing Au as the metallization material, one can maintain high conductivity while keeping the metallization layer thin to attain a high resolution.

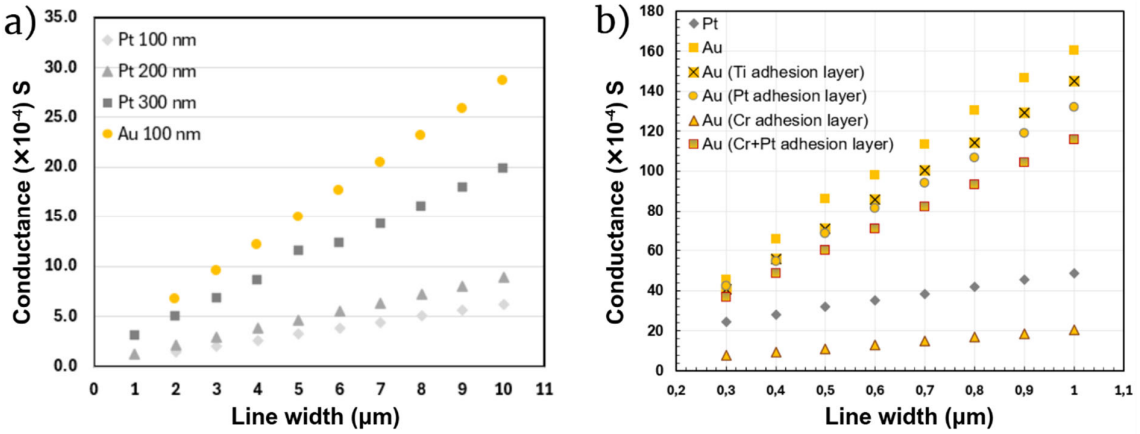

Figure 25. a) The measured conductance of Au and Pt with different thicknesses (100-300 nm) and line widths of 1-10 µm. b) The measured conductance of Pt and Au films with a sub-micrometer line width and various adhesion layers.

As line widths decrease, adhesion of the metallization and the substrate becomes increasingly critical due to the reduced interfacial area between the metal and the polymer substrate. Poor adhesion can result from weak interfacial bonding, which is exacerbated at smaller feature sizes. The conductance of sub-micrometer lines of Pt and Au (down to 0.3 μm) with various adhesion layers, is shown in Figure 25b. The 2PP test structure is shown in Figure 16 (Section 2.3.4.1).

As discussed in Section 2.1.3, Au exhibits poor adhesion to PI, necessitating the use of an adhesion layer beneath the Au. Cr, Ti, and Pt were tested here as adhesion layers for 2PP test structures. The adhesion layer is 10 nm for 100 nm thick Au, unless else stated. Although Pt does not formally function as an adhesion layer for Au, it generally adheres more strongly to PI than Au does. By depositing Pt underneath the Au, lift-off performance improved, resulting in higher fabrication yield for these structures. When using Pt as an adhesion layer, there was only a slight decrease in resistance.

The resistivity measurements showed that when using Ti as an adhesion layer, there is negligible decrease in conductivity and for Cr there is a substantial decrease in conductivity. The conductivity decrease could be due to the tendency of these materials to diffuse into Au during thermal processing, e.g. PI curing which reached up to 450°C, causing intermetallic formations[125,126]. Therefore, a diffusion barrier is required to prevent intermixing and preserve the electrical performance of the Au interconnects. Here, a 5 nm thick Pt layer was used to prevent diffusion of Cr (also 5 nm thick) into the Au, and as shown in the graph, the conductivity is only slightly lower compared to the Au with other adhesion layer.

Figure 26a and 26b further show that the impedance of Pt and Au electrodes depends on the line width of the interconnect leading to that electrode, which are clearly observable in the Bode-plot at frequencies above 100 Hz. This is expected as this is the region where the impedance will be dominated by the access resistance of the electrode rather than the phase-boundary. In this test, the electrodes (i.e., the material interfacing the electrolyte) were made of the same material as the interconnect lines with an electrode that is 500 μm in diameter (structure shown in Figure 15, Section 2.3.3.2). Because of the electrochemical properties of the material itself, only comparisons between different line widths within the same material are appropriate. These results indicate that interconnect geometry can significantly influence electrode impedance as line widths decrease.

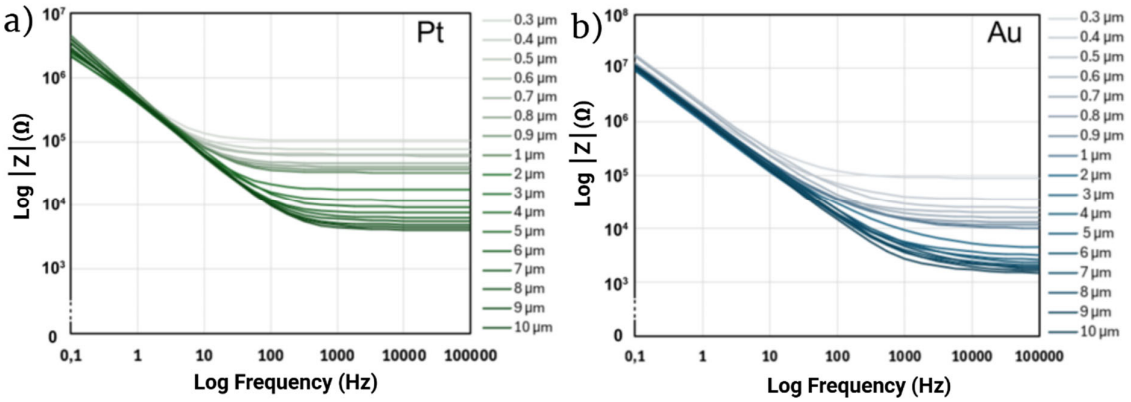

Figure 26. a) The impedance of Pt electrodes with varying line width (0.3-10 µm). Between 0.1-10 Hz there is no difference in impedance between these lines, and from 10 Hz and up there is a clear difference between the lines, for which the smaller line has higher impedance. The same goes on with Au electrodes in Figure b).

3.3 Miniaturization by using a hard mask

Multilayer implants can be achieved by connecting the metallization layers using a via structure (illustrated in Figure 27a), by connecting the electrode with a via structure (illustrated in Figure 27b) or by partly using recessed electrodes (shown in Figure 27c).

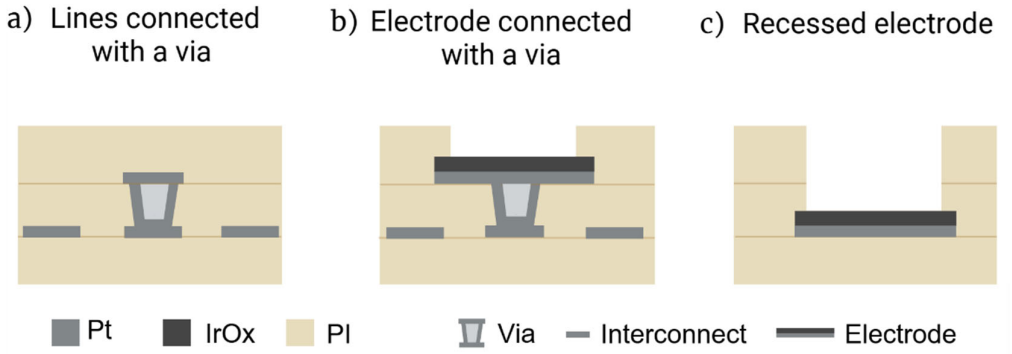

Figure 27. a) Various ways of fabricating multilayer implants. Two metallization layers can be fabricated using a via structure between interconnects, a via structure between interconnect and an electrode, or by etching deeper to reach the electrode.

Via structures were fabricated using the cross structures described in Figure 18 (Section 2.3.4.1), with a via incorporated at the center to assess its resistance. The fabricated structure is shown in Figure 28a, with a zoom in of SEM micrographs showing a via that measures 1.6

µm in diameter, with a PI thickness of 1.5 µm, giving an aspect ratio of almost 1:1. The intended via structure was 2 µm wide but resulted in a smaller opening.

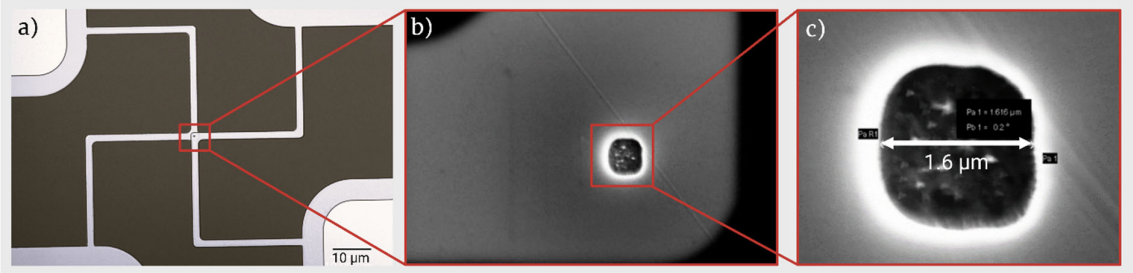

Figure 28. a) The fabricated cross structure used to measure the resistance in the via structure using 4PP measurement. b)-c) A fabricated via structure that is approximately 1.6 µm wide.

The fabrication process, illustrated in Figure 29a, begins with laser lithographic patterning, followed by deposition of a thin metal hard mask, made of thin-film Al (30 nm) and subsequently lift-off. The PI is etched to define the via openings, and the hard mask is thereafter removed by wet etching. The wafer is patterned again using laser lithography, and a second metallization layer is deposited by evaporation or sputtering, followed by lift-off. Finally, the top PI layer is deposited and cured. For electrical characterization, the contact pads of the cross structure are opened using RIE.

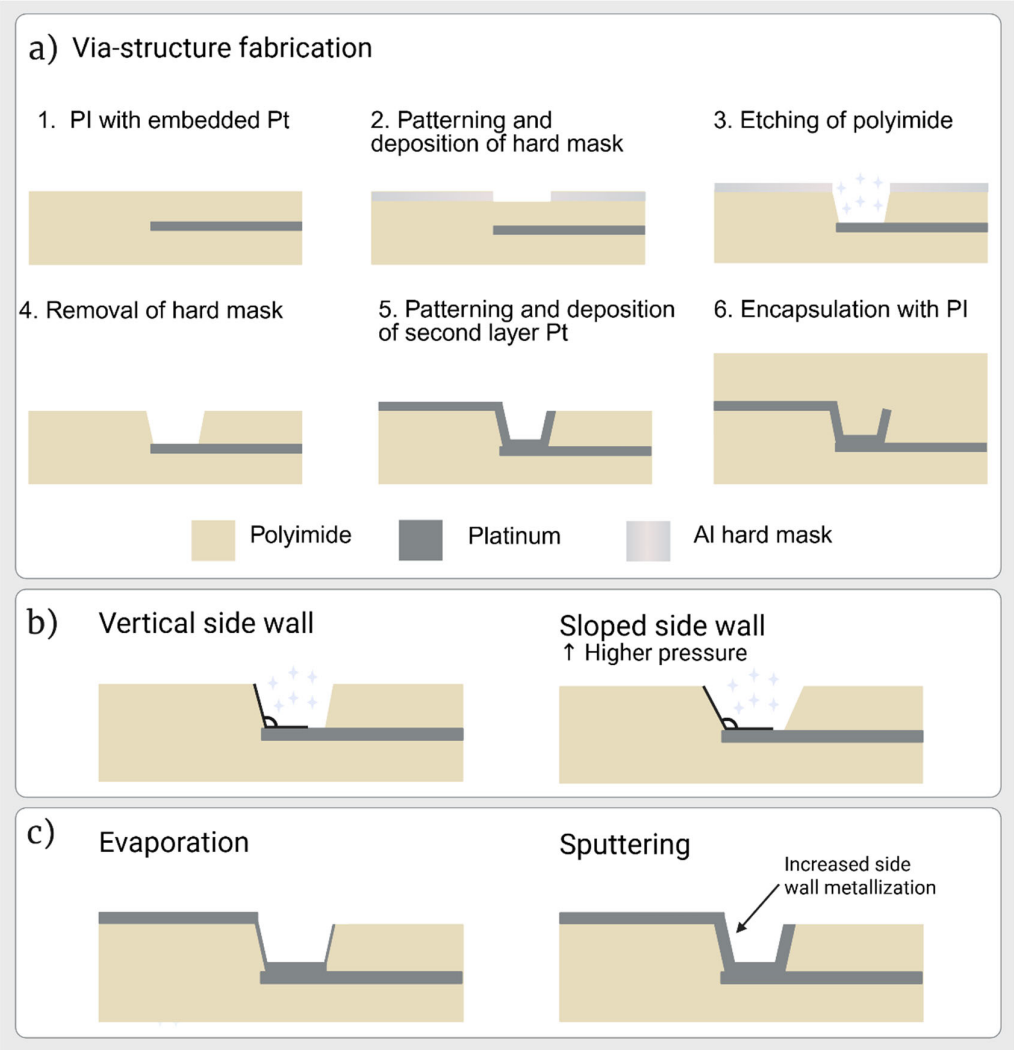

Figure 29. a) Schematic showing the fabrication process of via structure. To perform measurement, the pads of the structures are opened using RIE. b) Schematic showing how the side walls can be angled, to improve step coverage after metallization and thus reduce resistance. c) Schematic of how the metal deposition method affects the side wall metallization. When sputtering the metal is deposited on the side walls, decreasing the resistance in the via structure. When evaporating there is less metal on the side walls.

The measurement was conducted as described in Section 2.3.4.1 with an applied current sweep from 0 V to 0.5 V. The average resistance for via structures of diameters of 2, 5, 10, and 15 µm fabricated by evaporating the upper metal layer is shown in Figure 30a. As expected, the resistance decreases with increasing via diameter. This indicates that larger vias can be used to reduce resistance, but at the expense of increased area, which occupies more space on the implant.

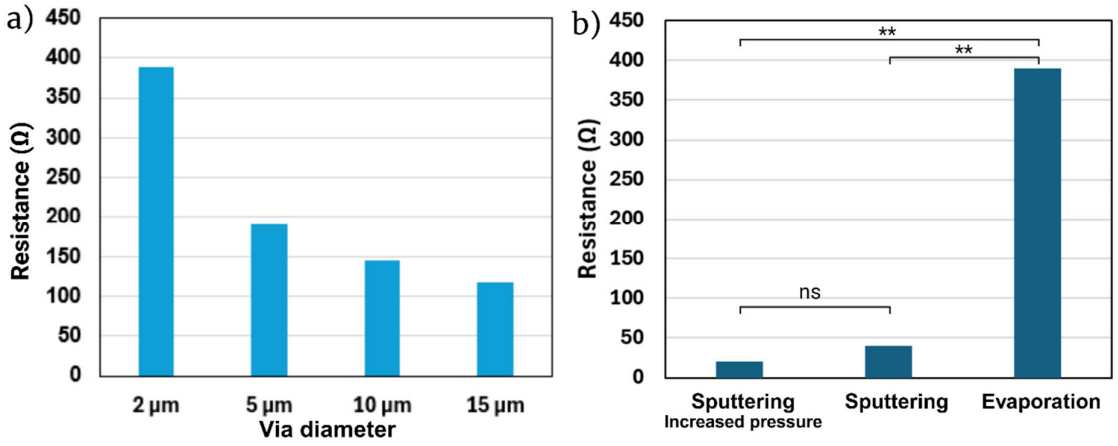

Figure 30. a) Measured resistance of via structures of different diameters. b) The measured resistance of via structures fabricated by normal and increased pressure, as well as different metallization routes. There is no significant difference in resistance between the sputtered samples with varying etching pressure, but there are significant differences between the sputtered samples and evaporated samples.

Achieving low-resistance contact between interconnected layers is critical in via fabrication, since poor contact in the via structure can negatively affect signal transmission. To ensure low resistance, there must be sufficient metallization along the via sidewalls to ensure reliable electrical connection between the layers. To improve the metallization coverage in the via structure, an increased sidewall slope can in theory help, although it could also negatively affect the resolution. Increasing the slope in the etched structures is accomplished by changing some parameters, for example pressure. With a higher chamber pressure the plasma molecules experience multiple collusions due to shorter mean free path, causing higher isotropy in the etching, resulting in higher slope[107] (illustrated in Figure 29b). Another method to increase the metal coverage within the via is to use sputter deposition instead of evaporation for the second metal layer, as it provides more conformal coating of the sidewalls (illustrated in Figure 29c).

Figure 30b shows the comparison of the resistance of vias fabricated at standard etching pressure and at slightly higher pressure, with a diameter around 2 µm (resulting via diameter is around 1.6 µm as shown in Figure 28c). The graph shows only small and statistically non-significant ($p=0.18$) differences between these groups. In contrast, a clear difference in resistance is observed between the evaporated and sputtered samples. The deviance between sputtered samples (at increased pressure) and evaporated samples is statistically significant ($p=0.0045$), as is the difference between sputtered and evaporated samples at standard

conditions (p=0.0067), based on Welch's t-test. Because of the reduced resistance when sputter-depositing the upper metal layer there could possibly be smaller difference in resistance between via diameters and smaller via structures can be facilitated without compromising the signal transmission.

3.3.1 Removal of hard mask

Figure 31 presents XPS measurements of the PI surface after removal of the Al hard mask. A potential concern with the etching process facilitated with a hard mask is that Al residues could remain on the surface and negatively affect adhesion of subsequent PI layers. However, the XPS data show no detectable Al peaks on the PI, indicating that the hard mask has been effectively removed and is unlikely to impact further processing or functionality on the finished device. However, this must be confirmed when etching thicker PI to open electrodes and pads and ensure no Al residues that can degrade the electrical and electrochemical contacts.

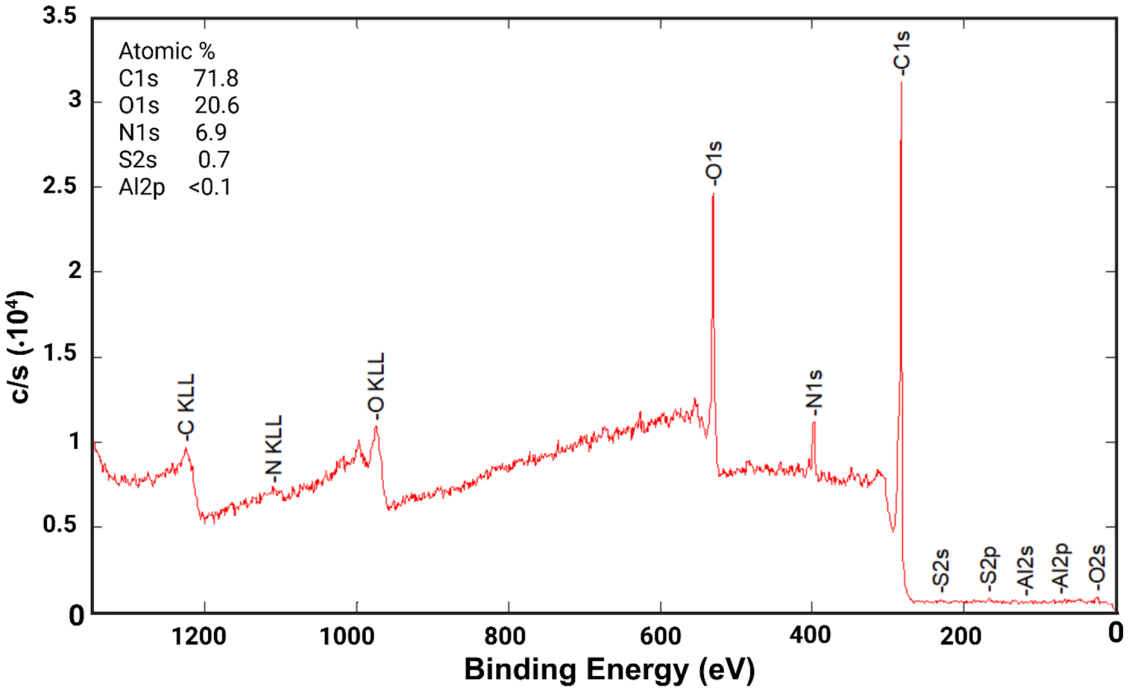

Figure 31. XPS data of PI after removal of the Al hard mask that shows no residual Al, confirming complete removal of the hard mask.

3.4 Miniaturization of implant volume

To reduce implant volume, thinner polymer layers must be fabricated, which can be achieved by diluting the polymer precursor solution. In this work, PI layers as thin as approximately 1

µm were obtained by spin-coating a solvent diluted PI solution (4:1 U-Varnish: NMP) at 7000 rpm on both 4-inch and 6-inch wafers, shown in Figure 32. This approach enables the realization of implants with total thicknesses of only a few micrometers.

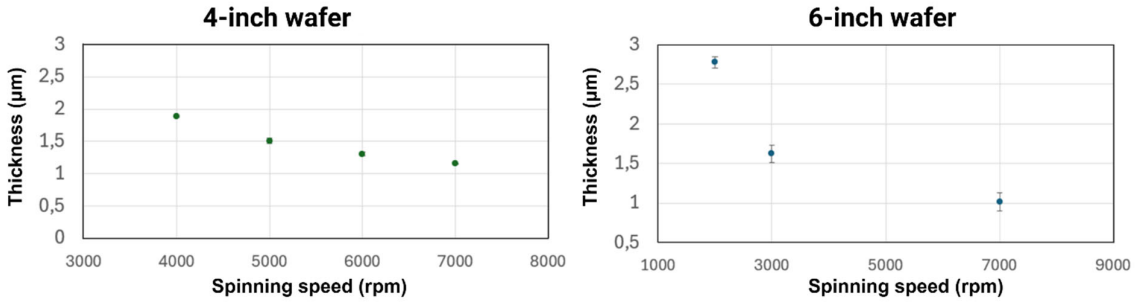

Figure 32. Spin curves of diluted PI (4:1 U-Varnish: NMP) on a 4-inch and 6-inch wafer.

3.5 Final result

A miniaturized straight TIME implant was designed with similar dimensions as the TIME implant presented in Section 1.3.1.2. The designed implant is shown in Figure 33. The EA site is 1 mm long and the electrodes have a dimension of 20×20 µm and a square shape, which chosen as it provides a low enough impedance to not jeopardize the function of the electrode, but still be small enough to be able to increase the amount of electrodes for improved signal selectivity and signal-to-noise ratio. The interconnects have a line width and pitch of 300 nm and 600 nm, respectively. These dimensions were chosen to ensure adhesion and a high fabrication yield of the metallized features during and after processing, and ensuring functionality of the electrodes. The designed device has 32 electrodes per arm, meaning 64 electrodes in total. The PI layers are only 1.5 µm thick, resulting in a total thickness of about 4.5 µm, and the width of the implant is 42 µm. These dimensions can be compared with previous clinically relevant TIME implant that is 200-280 µm wide, 11 µm thick and has 8-10 electrodes[65].

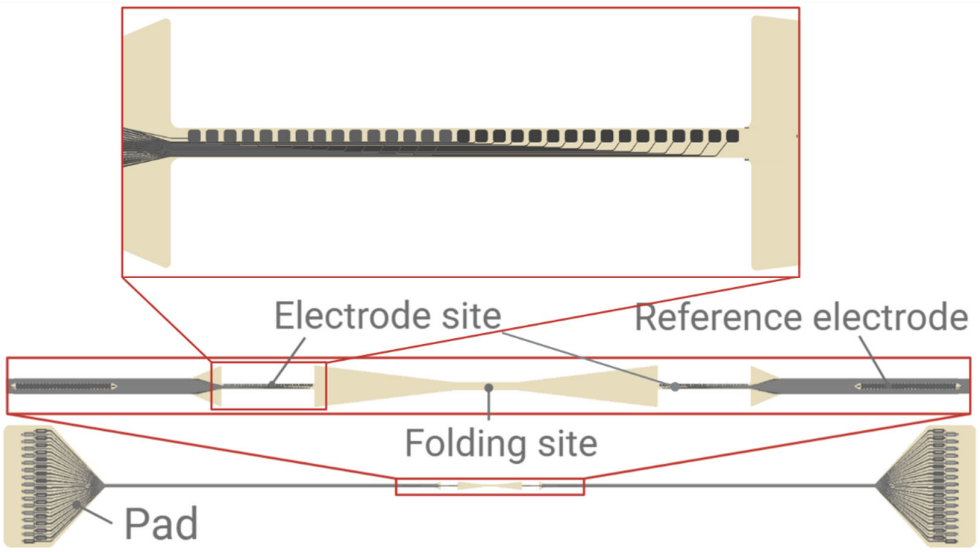

Figure 33. The designed miniaturized TIME implants, showing the pads, folding site, EA site and reference electrode.

The fabricated miniaturized TIME devices are shown in Figure 34a-c. This shows that fabricating a miniaturized TIME implant with substantially larger number of channels is possible by using the EBL processes developed in this work.

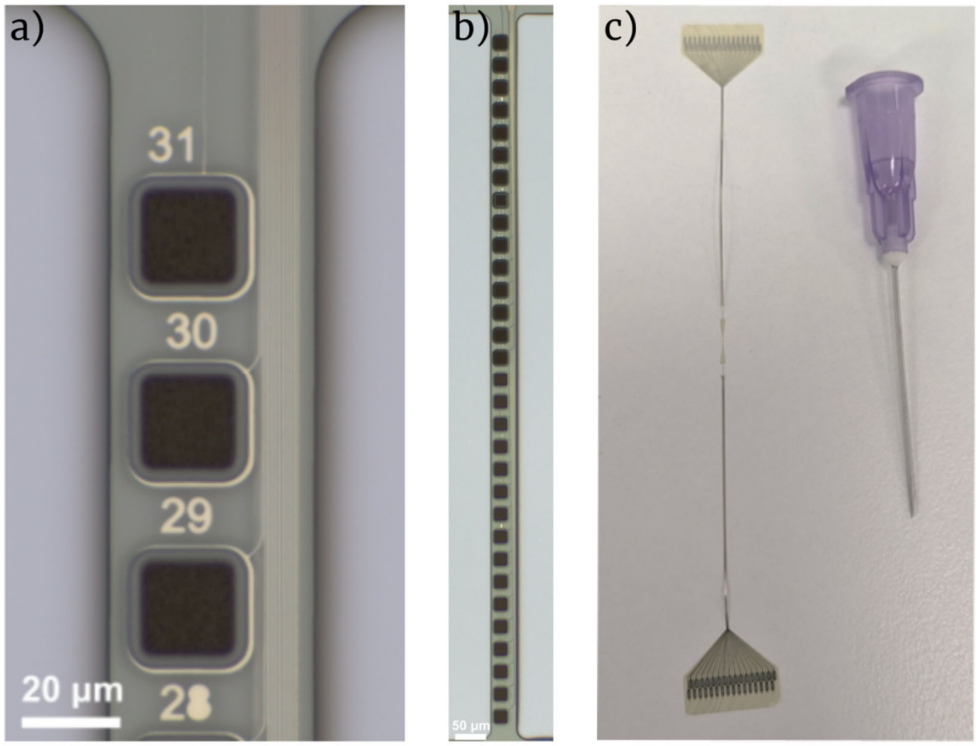

Figure 34. A zoom in of some of the electrodes on the fabricated TIME implant. c) The implanted section on the fabricated TIME implant. d) The complete TIME implant.

To investigate the effect of interconnect width and electrode size, a device was fabricated with line widths of 0.5 µm and 1 µm, incorporating electrodes distributed across two different layers. The overall device width is 105 µm, and the other dimensions are identical to those of the device presented in Figure 6 (Section 1.3.1.2). The complete device design is shown in Figure 35a, and the EA region is presented in the designed and fabricated devices in Figure 35b and 35c, respectively. A higher-magnification view of the fabricated EA region is provided in Figure 35d and 35e, showing the layered structures with interconnects beneath the electrodes. The implant contains 64 electrodes on each arm, of which 32 are connected to a zero-insertion-force connector, enabling effective in vivo testing while minimizing connector size. The electrodes are grouped depending on their electrode dimension and interconnect width. The four groups are electrodes that is 20×20 µm connected with a 0.5 µm line width, 20×20 µm connected with a 1 µm line width, 15×15 µm connected with a 0.5 µm line width and 15×15 µm connected with a 1 µm line width. The reduced line width is only in the EA site, elsewhere it is 3 µm wide. These are fabricated in two metallization layers, which means that two groups are recessed 7.5 µm beneath the implant surface and the other two groups are recessed 3.5 µm beneath the implant surface.

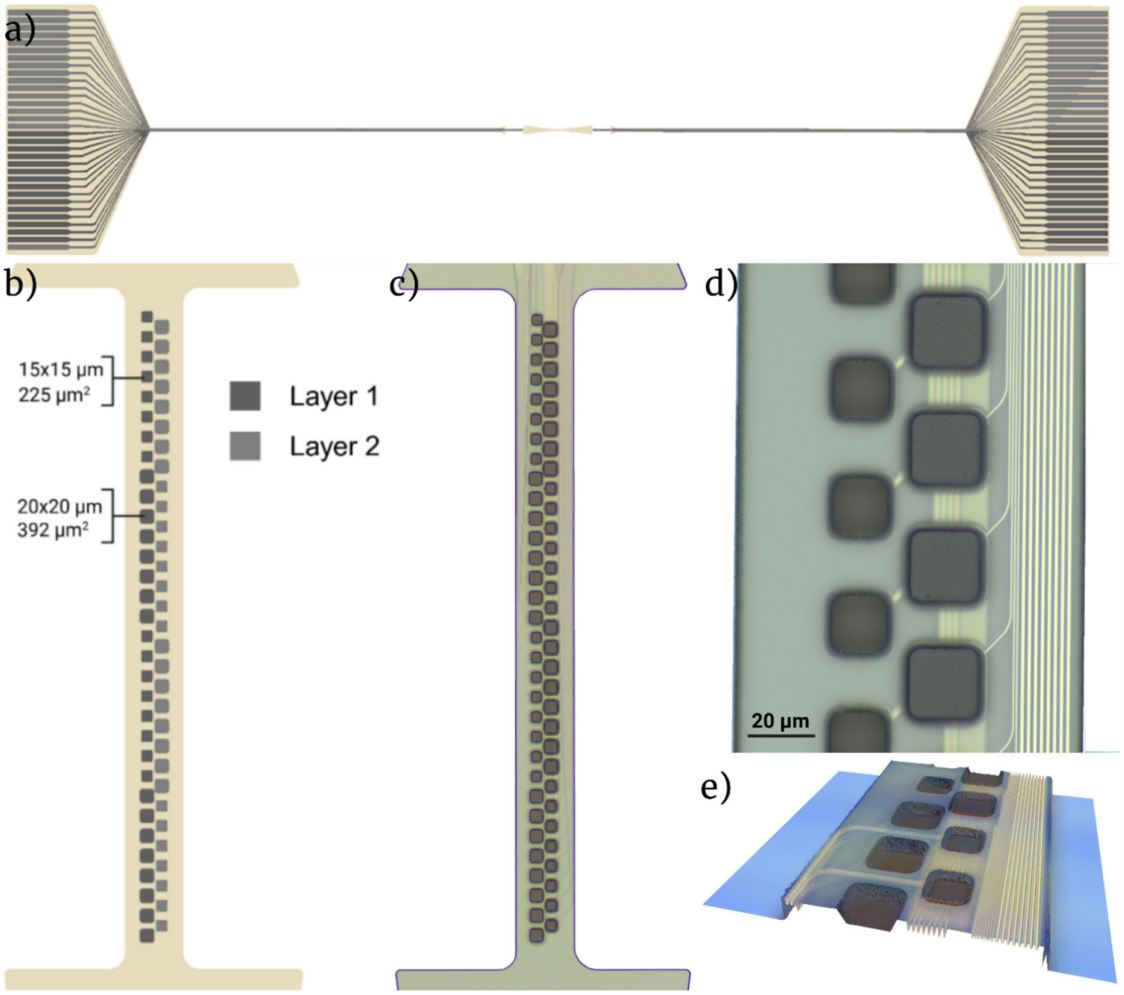

Figure 35. a) The whole designed TIME device. b) The ES of the designed device that has electrodes of two sizes in different metallization layers. b) The fabricated implant, showing the EA site. c) Zoom in of the electrodes showing the layered electrodes and interconnects of different dimensions. d) Figure acquired using an optical surface profilometer of the EA site, showing the depth of the electrodes in different layers. Picture credit: Ruggero Verre.

The measured impedance of each electrode group is shown in Figure 39a. Interestingly, in the frequency range between 0.1 and 100 Hz, the 20 µm electrodes exhibited the highest impedance. A possible explanation is that these electrodes are recessed by 7.5 µm (electrode layer 1), as illustrated in Figure 39b. The same recess depth is observed for the 15 µm electrodes with 0.5 µm line width. The increased recess depth may introduce a larger diffusion barrier and less accessible electrolyte, contributing to the higher impedance.

Otherwise, the electrodes show comparable impedance characteristics, particularly at frequencies above 100 Hz. At 1 kHz, which is the frequency with the highest relevance for

neural stimulation and recording, there is only a small difference between the grouped electrodes. For reference, the impedance of a 20 µm electrode with a 3 µm line width is included as a dashed line in the figure. These devices correspond to those presented in Figure 23 (Section 3.1).

Interestingly, the reference devices shown in gray line exhibit higher impedance compared to the other electrodes at low frequencies (0.1 Hz) but lower impedance compared to the other electrodes at higher frequencies (100 Hz). It should be noted that these electrodes are recessed by 6 µm, which can have an impact and makes direct comparison with the other samples difficult.

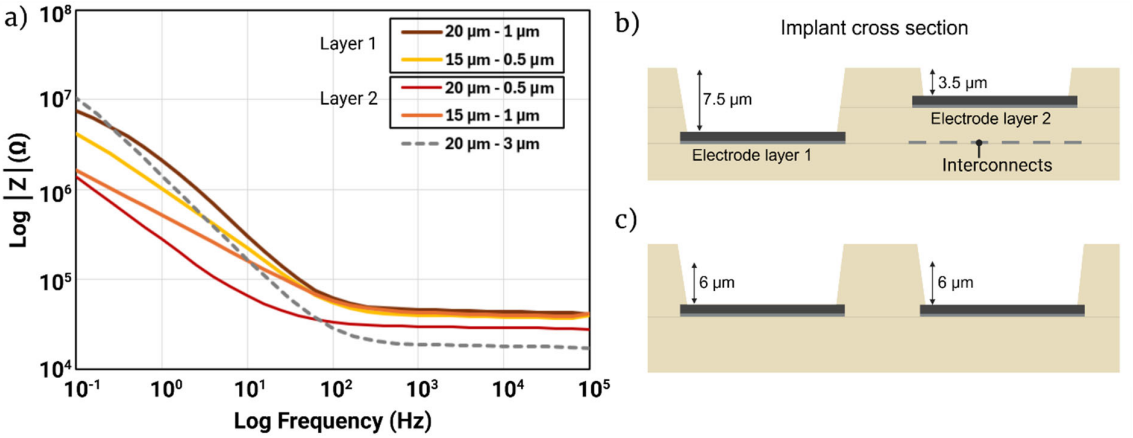

Figure 36. a) The measured impedance of the TIME device with varying electrode size and line width. The dashed grey line represents the measured impedance of another device without downscaled interconnects. b) The cross section of the fabricated multilayered TIME devices, showing the depth of the electrodes. Some electrodes are recessed 3.5 µm and some 7.5 µm. c) The placement of the electrodes on regular devices with 6 µm thick PI layers.

Discussion and conclusion

The aim of this work is to identify the key factors limiting the miniaturization of flexible neuroelectronic devices fabricated using EBL on polymer substrates, while enabling increased channel density and reduced implant volume through sub-micrometer interconnects and multilayer metallization.

As described in Paper A, from a fabrication perspective, the results demonstrate that EBL itself is not a primary limiting factor for patterning on PI substrate. Feature sizes down to 100 nm with pitches of 200 nm were achieved, and dense, reproducible arrays with 300 nm linewidth and 600 nm pitch were successfully fabricated. Contrary to commonly reported challenges for polymer substrates, such as charging and substrate damage[13], no significant issues were observed on PI. This suggests that under appropriate conditions, EBL is a viable and reliable technique for patterning on flexible substrates. These findings indicate that substrate-related process limitations are less restrictive than previously assumed, for substrates such as PI.

Moreover, as interconnect linewidth decreases, resistance increases significantly, making material selection and stack design critical. Au was identified as a favorable interconnect material due to its high conductivity, but the choice of adhesion layer was found to strongly influence overall electrical performance. In particular, Cr adhesion layers introduced diffusion-related conductivity losses, which could be mitigated by incorporating a Pt diffusion barrier. This highlights that, at the nanoscale, interfacial effects and material compatibility become key limiting factors for device performance.

Moreover, for multilayer architectures, via structures and multilayer devices introduce additional constraints. Sub-2 μm vias with aspect ratios of approximately 1:1 was successfully fabricated using hard-mask etching. While variations in etching parameters had limited impact on via resistance, the choice of metallization method proved critical. Sputter deposition significantly reduced via resistance compared to evaporation due to improved sidewall coverage. These results indicate that conformal coverage, rather than via geometry alone, is critical to achieve low resistance via structures that facilitate signal transmission between layers.

At the device level, the fabrication of a miniaturized, high-channel-count TIME implant demonstrates the feasibility of down scaling device dimensions using EBL. The realized device, featuring 300 nm interconnects, a two-layer architecture, and a total thickness of 4.5 μm, represents a substantial reduction compared to previously reported designs. However, this

scaling introduces new limitations related to electrical performance and mechanical stability. Increased interconnect resistance, reduced insulation thickness, and closer spacing between interconnects that increase the risk of crosstalk and reduced signal transmission. Additionally, thinner polyimide layers decrease mechanical robustness, posing challenges for implantation and long-term durability. For thinner polymer layers, a dissolvable film can be used to improve the mechanical strength of the implant to ensure implantation through the nerve tissue[127,128].

Electrochemical characterization further supports these observations. Devices with reduced interconnect dimensions exhibited slightly higher impedance compared to larger-feature counterparts, and differences between electrode layers were observed at lower frequencies. While performance at 1 kHz remained largely comparable, these results suggest that electrical performance reduces slightly as feature sizes approach the nanoscale for Pt interconnects. Thus, to overcome these challenges Au, would be a suitable alternative due to the increased conductivity.

Taken together, this work shows that the primary limitations for miniaturization of neuroelectronic devices using EBL on polymer substrates do not arise from the lithographic process itself, but rather from material interactions, electrical scaling effects, and mechanical constraints at reduced dimensions. While EBL enables the necessary resolution for high-density integration, achieving reliable and high-performance devices requires careful optimization of material stacks, deposition methods, and device architecture.

In conclusion, the work presented in this thesis enables the upscaling of implant channel density while simultaneously miniaturizing device volume. This advancement supports future long-term implantation of neural interfaces and facilitates stable bidirectional communication with the nervous system for BCI and BMI applications. By enabling miniaturized high-channel count interfaces, this line of research contributes to a future in which neuroprosthetic devices evolve from purely therapeutic tools into fully integrated devices of the human nervous system.

Outlook

Future work will focus on addressing the key material, electrical, and mechanical limitations identified in this thesis to enable miniaturization to push flexible neuroelectronic devices toward high-density, clinically viable systems. Improving metal adhesion remains critical as feature sizes decrease, and to further explore an optimized metal stack, the adhesive layers should be tested systematically and quantified. In addition, the transition from Pt to Au as an interconnect material requires careful optimization of adhesion layers to ensure compatibility with subsequently deposited IrOx.

A systematic comparison between lift-off and etching-based processes, combined with different deposition methods such as evaporation and sputtering, will be conducted to evaluate their impact on adhesion strength, electrical performance, and long-term stability. While lift-off offers high patterning flexibility, sputtering provides improved film conformity and adhesion to the substrate, making it a promising approach for nanoscale interconnects.

As interconnect spacing decreases and multilayer architectures become more complex, crosstalk between adjacent conductors, both laterally and across layers, emerges as a critical limitation. Future studies should therefore focus on quantifying these effects and developing strategies to mitigate them through optimized device layout and material selection. Moreover, the introduction of additional insulating or adhesion-promoting layers, such as silicon carbide, may further improve both electrical isolation and structural integrity.

Mechanical stability also becomes increasingly important as device thickness is reduced. Thinner polyimide layers improve flexibility but introduce fragility, which can compromise device integrity during implantation, particularly for applications such as TIME implants that require sew-in insertion into the nerve tissue. Strategies to reinforce the device, such as dissolvable coatings, should be explored to ensure reliable implantation. Additionally, as the total material volume decreases, the device becomes more sensitive to degradation mechanisms, including swelling, delamination, and surface modification, which can rapidly impact overall performance. Therefore, aging test of these devices is critical to ensure long-term stability comparable with the current devices.

Finally, in vivo validation represents a crucial next step. Comparative studies between miniaturized TIME implants and larger, higher-channel-count devices will enable evaluation of both functional performance and biological response. Emphasis should be placed on assessing signal selectivity, signal-to-noise ratio, and long-term stability, as well as the FBR

following implantation in the rat sciatic nerve. These investigations will be essential to determine whether the advantages of miniaturization translate into improved performance and clinical viability.

In a broader perspective, overcoming these challenges will move the field closer to seamless integration between electronic systems and the nervous system. By enabling dense, stable, and minimally invasive interfaces, this line of research contributes to a future where neuroprosthetic devices are not only therapeutic tools but fully integrated components of the human body.

Future work should therefore focus on comprehensive electrical and biological validation of these miniaturized devices, including long-term stability, foreign body response, signal selectivity, and signal-to-noise ratio. Addressing these aspects will be essential to ensure that the benefits of miniaturization and up-scaling of channels translate into improved performance and clinical viability for next-generation neural interfaces.

Acknowledgement

During my years as a Ph.D. student, I have been fortunate to be surrounded by many supportive colleagues and friends.

First and foremost, I would like to thank my supervisor, Maria Asplund, for giving me the opportunity to pursue a Ph.D. in her group, for introducing me to the field of neural engineering and supporting me in this journey. I am also grateful to my co-supervisor, Per Rudquist, for his guidance and valuable discussions throughout this work.

I would like to thank my examiner and colleague, Johan Liu, for his extensive support leading up to this licentiate thesis, as well as Per Lundgren for his guidance in his role as Director of Studies and as a colleague.

I am deeply thankful to my colleagues in the Bioelectronics group for their support, collaboration, and friendship: Lukas Matter, Shahrzad Damerceli, Matilda Öjmertz, Gonzalo Gonzalez, José Leal, Karin Hedsten and Mehmet G. Say. I would also like to extend my thanks to all current and former colleagues at EMSL.

My sincere thanks go to the NFL, CMAL and IMS staff, who make high-quality research possible. Your support and willingness to help have been invaluable. I would especially like to thank Niclas Lindvall, Ruggero Verre and Eric Tam for sharing their expertise in micro- and nanofabrication and analytical methods, and for always going the extra mile for me.

I am also grateful to the many colleagues and friends at MC2, many, but not all, of whom I initially met in the cleanroom. You made my time there both more enjoyable and more enriching through engaging conversations and new perspectives.

Finally, I would like to thank my family and friends for their constant support and encouragement throughout this journey, and especially Calle for his patience, love, and unwavering support.

References

1. Zhang, H. *et al.* Brain–computer interfaces: the innovative key to unlocking neurological conditions. *Int. J. Surg.* **110**, 5745–5762 (2024).

2. Hassler, C., Boretius, T. & Stieglitz, T. Polymers for neural implants. *J. Polym. Sci. Part B Polym. Phys.* **49**, 18–33 (2011).

3. Awuah, W. A. *et al.* Bridging Minds and Machines: The Recent Advances of Brain-Computer Interfaces in Neurological and Neurosurgical Applications. *World Neurosurg.* **189**, 138–153 (2024).

4. Harland, B. *et al.* Daily electric field treatment improves functional outcomes after thoracic contusion spinal cord injury in rats. *Nat. Commun.* **16**, 5372 (2025).

5. Deng, Q., Fu, Z., Ma, N. & Wang, B. Application and future directions of brain-computer interfaces in neurological disorders: Technological advances, clinical practices, and challenges. *Brain Hemorrhages* **6**, 306–314 (2025).

6. Lefebvre, P. P., Müller, J., Mark, G., Schwarze, F. & Hochmair, I. Rehabilitation of human hearing with a totally implantable cochlear implant: a feasibility study. *Commun. Med.* **5**, 10 (2025).

7. Warwick, K. Neuroengineering and neuroprosthetics. *Brain Neurosci. Adv.* **2**, (2018).

8. Fernandez, E. Development of visual Neuroprostheses: trends and challenges. *Bioelectron. Med.* **4**, 12 (2018).

9. Boehler, C., Carli, S., Fadiga, L., Stieglitz, T. & Asplund, M. Tutorial: guidelines for standardized performance tests for electrodes intended for neural interfaces and bioelectronics. *Nat. Protoc.* **15**, 3557–3578 (2020).

10. Musk, E. An Integrated Brain-Machine Interface Platform With Thousands of Channels. *J. Med. Internet Res.* **21**, e16194 (2019).

11. Slutzky, M. W. Brain-Machine Interfaces: Powerful Tools for Clinical Treatment and Neuroscientific Investigations. *Neurosci.* **25**, 139–154 (2019).

12. Kuliasha, C. A. & Judy, J. W. The Materials Science Foundation Supporting the Microfabrication of Reliable Polyimide–Metal Neuroelectronic Interfaces. *Adv. Mater. Technol.* **6**, (2021).

13. Scholten, K. & Meng, E. Electron-beam lithography for polymer bioMEMS with submicron features. *Microsystems Nanoeng.* **2**, 16053 (2016).

14. Altuna, A., Berganzo, J. & Fernández, L. J. Polymer SU-8-Based Microprobes for Neural Recording and Drug Delivery. *Front. Mater.* **2**, (2015).

15. Sifringer, L. *et al.* An Implantable Biohybrid Neural Interface Toward Synaptic Deep Brain Stimulation. *Adv. Funct. Mater.* **35**, (2025).

16. Wang, Y., Liu, S., Wang, H., Zhao, Y. & Zhang, X.-D. Neuron devices: emerging prospects in neural interfaces and recognition. *Microsystems Nanoeng.* **8**, 128 (2022).

17. Lotti, F., Ranieri, F., Vadalà, G., Zollo, L. & Di Pino, G. Invasive Intraneural Interfaces: Foreign Body Reaction Issues. *Front. Neurosci.* **11**, (2017).

18. Steinmetz, N. A. *et al.* Neuropixels 2.0: A miniaturized high-density probe for stable,

long-term brain recordings. *Science (80-.).* **372**, (2021).

19. Koschinski, L. *et al.* High-Density Flexible Neural Implants with Submicron Feedline Resolution. *Adv. Electron. Mater.* **11**, (2025).

20. Böhler, C. *et al.* Multilayer Arrays for Neurotechnology Applications (MANTA): Chronically Stable Thin-Film Intracortical Implants. *Adv. Sci.* **10**, (2023).

21. Ludwig, P. E., Reddy, V. & Varacallo, M. A. *Neuroanatomy, Central Nervous System (CNS)(Archived)*. (2026).

22. Mai, J. K. . & Paxinos, G. *The Human Nervous System*. (Elsevier Academic Press, 2012).

23. Wang, Y. Creating Ultrafast Biosensors for Neuroscience . (Chalmers University of Technology, Gothenburg, 2019).

24. Maton, A. *Human Biology and Health*. (Prentice Hall, 1993).

25. Saladin, K. S. . *Anatomy & Physiology : The Unity of Form and Function*. (McGraw Hill LLC, 2024).

26. Matic, A. I. Introduction to the Nervous System, Part 2: The Autonomic Nervous System and the Central Nervous system. (2014).

27. Siegel, G. J., Agranoff, B. W., Albers, W. R. & Molinoff, P. B. *Basic Neurochemistry*. (Raven Press, 1994).

28. Sleigh, J. N. Editorial: Peripheral nerve anatomy in health and disease. *J. Anat.* **241**, 1083–1088 (2022).

29. Fallon, M. & Tadi, P. *Histology, Schwann Cells*. (2026).

30. Yan, L. *et al.* An experimental and numerical study of the microstructural and biomechanical properties of human peripheral nerve endoneurium for the design of tissue scaffolds. *Front. Bioeng. Biotechnol.* **10**, (2022).

31. Brill, N. A. & Tyler, D. J. Quantification of human upper extremity nerves and fascicular anatomy. *Muscle Nerve* **56**, 463–471 (2017).

32. Layton, B. E. & Sastry, A. M. A Mechanical Model for Collagen Fibril Load Sharing in Peripheral Nerve of Diabetic and Nondiabetic Rats. *J. Biomech. Eng.* **126**, 803–814 (2004).

33. Hope, J., Braeuer, B., Amirapu, S., McDaid, A. & Vanholsbeeck, F. Extracting morphometric information from rat sciatic nerve using optical coherence tomography. *J. Biomed. Opt.* **23**, 1 (2018).

34. Fortin, J. S., Chlipala, E. A., Shaw, D. P. & Bolon, B. Methods Optimization for Routine Sciatic Nerve Processing in General Toxicity Studies. *Toxicol. Pathol.* **48**, 19–29 (2020).

35. Karkanitsa, M., Fathi, P., Ngo, T. & Sadtler, K. Mobilizing Endogenous Repair Through Understanding Immune Reaction With Biomaterials. *Front. Bioeng. Biotechnol.* **9**, (2021).

36. Onuki, Y., Bhardwaj, U., Papadimitrakopoulos, F. & Burgess, D. J. A Review of the Biocompatibility of Implantable Devices: Current Challenges to Overcome Foreign Body Response. *J. Diabetes Sci. Technol.* **2**, 1003–1015 (2008).

37. Williams, D. F. On the mechanisms of biocompatibility. *Biomaterials* **29**, 2941–2953 (2008).

38. Capuani, S., Malgir, G., Chua, C. Y. X. & Grattoni, A. Advanced strategies to thwart foreign body response to implantable devices. *Bioeng. Transl. Med.* **7**, (2022).

39. Kanďárová, H. & Pôbiš, P. The "Big Three" in biocompatibility testing of medical devices: implementation of alternatives to animal experimentation—are we there yet? *Front. Toxicol.* **5**, (2024).

40. Karakurt, E. M. *et al.* Assessing Microstructural, Biomechanical, and Biocompatible Properties of TiNb Alloys for Potential Use as Load-Bearing Implants. *J. Funct. Biomater.* **15**, 253 (2024).

41. Tang, L., Thevenot, P. & Hu, W. Surface Chemistry Influences Implant Biocompatibility. *Curr. Top. Med. Chem.* **8**, 270–280 (2008).

42. Turrin, G. *et al.* Covalent Binding of Dexamethasone to Polyimide Improves Biocompatibility of Neural Implantable Devices. *Adv. Healthc. Mater.* **14**, (2025).

43. Badia, J. *et al.* Biocompatibility of Chronically Implanted Transverse Intrafascicular Multichannel Electrode (TIME) in the Rat Sciatic Nerve. *IEEE Trans. Biomed. Eng.* **58**, 2324–2332 (2011).

44. Perna, A., Angotzi, G. N., Berdondini, L. & Ribeiro, J. F. Advancing the interfacing performances of chronically implantable neural probes in the era of CMOS neuroelectronics. *Front. Neurosci.* **17**, (2023).

45. de la Oliva, N., Navarro, X. & del Valle, J. Time course study of long-term biocompatibility and foreign body reaction to intraneural polyimide-based implants. *J. Biomed. Mater. Res. Part A* **106**, 746–757 (2018).

46. Eluagu, C. C., Biney, B. W., Cogan, S. F., Otto, K. J. & Orazem, M. E. Electrochemical impedance spectroscopy for characterizing neural electrodes. *Curr. Opin. Electrochem.* **56**, 101807 (2026).

47. Le, X., Poinern, G. E. J., Ali, N., Berry, C. M. & Fawcett, D. Engineering a Biocompatible Scaffold with Either Micrometre or Nanometre Scale Surface Topography for Promoting Protein Adsorption and Cellular Response. *Int. J. Biomater.* **2013**, 1–16 (2013).

48. Xu, L.-C. & Siedlecki, C. A. Surface texturing and combinatorial approaches to improve biocompatibility of implanted biomaterials. *Front. Phys.* **10**, (2022).

49. Orlemann, C. *et al.* Friend, Not Foe: Lowered Tissue Reactivity to Long-Term Polyimide Implants. *Adv. Sci.* https://doi.org/10.1002/advs.202600028 (2026) doi:10.1002/advs.202600028.

50. Otte, E., Vlachos, A. & Asplund, M. Engineering strategies towards overcoming bleeding and glial scar formation around neural probes. *Cell Tissue Res.* **387**, 461–477 (2022).

51. Ezeokafor, I., Upadhya, A. & Shetty, S. Neurosensory Prosthetics: An Integral Neuromodulation Part of Bioelectronic Device. *Front. Neurosci.* **15**, (2021).

52. Hughes, C. L., Stieger, K. C., Chen, K., Vazquez, A. L. & Kozai, T. D. Y.

Spatiotemporal properties of cortical excitatory and inhibitory neuron activation by sustained and bursting electrical microstimulation. *iScience* **28**, 112707 (2025).

53. Cogan, S. F. Neural Stimulation and Recording Electrodes. *Annu. Rev. Biomed. Eng.* **10**, 275–309 (2008).

54. Sillay, K. A. *et al.* Long-Term Measurement of Impedance in Chronically Implanted Depth and Subdural Electrodes During Responsive Neurostimulation in Humans. *Brain Stimul.* **6**, 718–726 (2013).

55. Cisnal, A. *et al.* A Measurement Setup and Automated Calculation Method to Determine the Charge Injection Capacity of Implantable Microelectrodes. *Sensors* **18**, 4152 (2018).

56. Matter, L., Abdullaeva, O. S., Shaner, S., Leal, J. & Asplund, M. Bioelectronic Direct Current Stimulation at the Transition Between Reversible and Irreversible Charge Transfer. *Adv. Sci.* **11**, (2024).

57. Brunton, E. K. *et al.* In vivo comparison of the charge densities required to evoke motor responses using novel annular penetrating microelectrodes. *Front. Neurosci.* **09**, (2015).

58. Ullah, N. & Omanovic, S. Large charge-storage-capacity iridium/ruthenium oxide coatings as promising material for neural stimulating electrodes. *Mater. Chem. Phys.* **159**, 119–127 (2015).

59. McGlynn, E. *et al.* The Future of Neuroscience: Flexible and Wireless Implantable Neural Electronics. *Adv. Sci.* **8**, (2021).

60. Lozano, A. M. *et al.* Deep brain stimulation: current challenges and future directions. *Nat. Rev. Neurol.* **15**, 148–160 (2019).

61. Hettick, M. *et al.* Minimally invasive implantation of scalable high-density cortical microelectrode arrays for multimodal neural decoding and stimulation. *Nat. Biomed. Eng.* https://doi.org/10.1038/s41551-025-01501-w (2025) doi:10.1038/s41551-025-01501-w.

62. Jeon, Y. H. Spinal Cord Stimulation in Pain Management: A Review. *Korean J. Pain* **25**, 143–150 (2012).

63. Deep, N., Choudhury, B. & Roland, J. Auditory Brainstem Implantation: An Overview. *J. Neurol. Surg. Part B Skull Base* **80**, 203–208 (2019).

64. Fisher, L. E., Gaunt, R. A. & Huang, H. Sensory restoration for improved motor control of prostheses. *Curr. Opin. Biomed. Eng.* **28**, 100498 (2023).

65. Boretius, T. *et al.* A transverse intrafascicular multichannel electrode (TIME) to interface with the peripheral nerve. *Biosens. Bioelectron.* **26**, 62–69 (2010).

66. Rijnbeek, E. H., Eleveld, N. & Olthuis, W. Update on Peripheral Nerve Electrodes for Closed-Loop Neuroprosthetics. *Front. Neurosci.* **12**, (2018).

67. Tyler, D. J. & Durand, D. M. A slowly penetrating interfascicular nerve electrode for selective activation of peripheral nerves. *IEEE Trans. Rehabil. Eng.* **5**, 51–61 (1997).

68. Stieglitz, T. Flexible biomedical microdevices with double-sided electrode arrangements for neural applications. *Sensors Actuators A Phys.* **90**, 203–211 (2001).

69. Cheng, J., Yang, Z., Overstreet, C. K. & Keefer, E. Fascicle-Specific Targeting of

Longitudinal Intrafascicular Electrodes for Motor and Sensory Restoration in Upper-Limb Amputees. *Hand Clin.* **37**, 401–414 (2021).

70. Badia, J. *et al.* Comparative analysis of transverse intrafascicular multichannel, longitudinal intrafascicular and multipolar cuff electrodes for the selective stimulation of nerve fascicles. *J. Neural Eng.* **8**, 036023 (2011).

71. European Commision. BioFunctional IntraNeural Electrodes.

72. Golda-Cepa, M., Engvall, K., Hakkarainen, M. & Kotarba, A. Recent progress on parylene C polymer for biomedical applications: A review. *Prog. Org. Coatings* **140**, 105493 (2020).

73. Kim, B. J., Washabaugh, E. P. & Meng, E. Annealing effects on flexible multi-layered parylene-based sensors. in *2014 IEEE 27th International Conference on Micro Electro Mechanical Systems (MEMS)* 825–828 (IEEE, 2014). doi:10.1109/MEMSYS.2014.6765768.

74. González, J. P.-P., Lamure, A. & Senocq, F. Polyimide (PI) films by chemical vapor deposition (CVD): Novel design, experiments and characterization. *Surf. Coatings Technol.* **201**, 9437–9441 (2007).

75. Wang, R. *et al.* Fabrication and Characterization of a Parylene-Based Three-Dimensional Microelectrode Array for Use in Retinal Prosthesis. *J. Microelectromechanical Syst.* **19**, 367–374 (2010).

76. Wang, X. *et al.* A Parylene Neural Probe Array for Multi-Region Deep Brain Recordings. *J. Microelectromech. Syst.* **29**, 499–513 (2020).

77. Schander, A., Gancz, J., Tintelott, M. & Lang, W. Towards Long-Term Stable Polyimide-Based Flexible Electrical Insulation for Chronically Implanted Neural Electrodes. *Micromachines* **12**, 1279 (2021).

78. UBE. U-Varnish-S, -A.

79. Raspopovic, S., Valle, G. & Petrini, F. M. Sensory feedback for limb prostheses in amputees. *Nat. Mater.* **20**, 925–939 (2021).

80. Miranda, I. *et al.* Properties and Applications of PDMS for Biomedical Engineering: A Review. *J. Funct. Biomater.* **13**, 2 (2021).

81. Chen, Z. & Lee, J.-B. Biocompatibility of SU-8 and Its Biomedical Device Applications. *Micromachines* **12**, 794 (2021).

82. Rihani, R. *et al.* Liquid Crystalline Polymers: Opportunities to Shape Neural Interfaces. *Neuromodulation Technol. Neural Interface* **25**, 1259–1267 (2022).

83. Chakraborty, B., Joshi-Imre, A. & Cogan, S. F. Charge injection characteristics of sputtered ruthenium oxide electrodes for neural stimulation and recording. *J. Biomed. Mater. Res. Part B Appl. Biomater.* **110**, 229–238 (2022).

84. Frederick, R. A., Meliane, I. Y., Joshi-Imre, A., Troyk, P. R. & Cogan, S. F. Activated iridium oxide film (AIROF) electrodes for neural tissue stimulation. *J. Neural Eng.* **17**, 056001 (2020).

85. Cogan, S. F. *et al.* Sputtered iridium oxide films for neural stimulation electrodes. *J. Biomed. Mater. Res. Part B Appl. Biomater.* **89B**, 353–361 (2009).

86. Serway, R. A. . *Principles of Physics*. (Saunders College Pub., 1998).

87. Boehler, C., Stieglitz, T. & Asplund, M. Nanostructured platinum grass enables superior impedance reduction for neural microelectrodes. *Biomaterials* **67**, 346–353 (2015).

88. Tiwari, C. S. *et al.* Characterization of the Descum Process for Various Silicon Substrates Doping. *ECS Trans.* **58**, 251–259 (2013).

89. Zaouk, R., Park, B. Y. & Madou, M. J. Introduction to Microfabrication Techniques. in *Microfluidic Techniques* 3–16 (Humana Press, New Jersey). doi:10.1385/1-59259-997-4:3.

90. Madou, M. J. . *Fundamentals of Microfabrication : The Science of Miniaturization*. (CRC Press, 2002).

91. Jain, R. *Advancements in AI and IoT for Chip Manufacturing and Defect Prevention*. (River Publishers, 2024).

92. Rai-Choudhury, P. *Handbook of Microlithography, Micromachining, and Microfabrication. Volume 1: Microlithography*. (SPIE PRESS, 1997). doi:10.1117/3.2265070.

93. Cui, Z. *Nanofabrication*. (Springer US, Boston, MA, 2008). doi:10.1007/978-0-387-75577-9.

94. Kitsara, M., Kontziampasis, D., Agbulut, O. & Chen, Y. Heart on a chip: Micro-nanofabrication and microfluidics steering the future of cardiac tissue engineering. *Microelectron. Eng.* **203**–**204**, 44–62 (2019).

95. Lin, B. J. Immersion Lithography. in *Optical Lithography: Here is Why, Second Edition* (SPIE, 2021). doi:10.1117/3.2586123.ch8.

96. UCSB NanoFab. Contact Aligner (SUSS MA-6). (2025).

97. Ronse, K., Hendrickx, E., Goethals, M., Jonckheere, R. & Vandenberghe, G. Status and challenges of extreme-UV lithography. in *2009 International Symposium on VLSI Technology, Systems, and Applications* 98–99 (IEEE, 2009). doi:10.1109/VTSA.2009.5159309.

98. Lian, Y. *Semiconductor Microchips and Fabrication : A Practical Guide to Theory and Manufacturing*. (Wiley-IEEE Press, 2023).

99. Heidelberg Instruments. Direct Writing for Microfabrication and Rapid Prototyping.

100. Lindroos, V. *Handbook of Silicon Based MEMS : Materials & Technologies*. (William Andrew, 2015).

101. Heidelberg instruments. MLA 150 Maskless Aligner.

102. Heidelberg Instruments. DWL 2000 GS / DWL 4000 GS Laser Lithography Systems.

103. Cabrini, S. & Kawata, S. *Nanofabrication Handbook*. (CRC Press, 2012).

104. Awan, T. I., Afsheen, S. & Kausar, S. *Thin Film Deposition Techniques*. (Springer Nature Singapore, Singapore, 2025). doi:10.1007/978-981-96-1364-9.

105. Jiang, W., Ide, K., Kitayama, S., Suzuki, T. & Yatsui, K. Pulsed Ion-Beam Evaporation for Thin-Film Deposition. *Jpn. J. Appl. Phys.* **40**, 1026 (2001).

106. Shan, H. *et al. Reactive Ion Etching of Polymers: On Photoresist Faceting, Underlayer Selectivity, and Oxide Etch Fundamentals*.

107. Huff, M. Recent Advances in Reactive Ion Etching and Applications of High-Aspect-Ratio Microfabrication. *Micromachines* **12**, 991 (2021).

108. Drost, M. *et al.* Etch mechanism of an Al2O3 hard mask in the Bosch process. *Micro Nano Eng.* **14**, 100102 (2022).

109. Khamnualthong, N., Siangchaew, K. & Limsuwan, P. Study of Chromium Hard Mask Formation and Wall Angle Control for Deep Etching Application. *Procedia Eng.* **32**, 922–928 (2012).

110. Jovanović, J., Milosavljević, S., Nanver, L. K., Suligoj, T. & Biljanovic, P. Sub-100 nm silicon-nitride hard-mask for high aspect-ratio silicon fins. in *MIPRO 2007 - 30th Jubilee International Convention: Microelectronics, Electronics and Electronic Technologies, Hypermedia and Grid Systems, MEET /HGS* (Opatija, Croatia, 2007).

111. Delprat, S., Chaker, M. & Margot, J. Patterned Platinum Etching Studies in an Argon High-Density Plasma. *Jpn. J. Appl. Phys.* **38**, 4488 (1999).

112. Racka-Szmidt, K., Stonio, B., Żelazko, J., Filipiak, M. & Sochacki, M. A Review: Inductively Coupled Plasma Reactive Ion Etching of Silicon Carbide. *Materials (Basel).* **15**, 123 (2021).

113. Reimer, L. *Scanning Electron Microscopy : Physics of Image Formation and Microanalysis*. (Springer-Verlag, 1985).

114. Racz, A. S. & Menyhard, M. Evaluation methods for XPS depth profiling; A review. *Appl. Surf. Sci. Adv.* **30**, 100872 (2025).

115. Moulder, J. F. . & Chastain, J. *Handbook of X-Ray Photoelectron Spectroscopy : A Reference Book of Standard Spectra for Identification and Interpretation of XPS Data*. (Physical Electronics Division, Perkin-Elmer Corp., 1992).

116. Elgrishi, N. *et al.* A Practical Beginner's Guide to Cyclic Voltammetry. *J. Chem. Educ.* **95**, 197–206 (2018).

117. Wilks, S. J. *et al.* Voltage Biasing, Cyclic Voltammetry, & Electrical Impedance Spectroscopy for Neural Interfaces. *J. Vis. Exp.* https://doi.org/10.3791/3566 (2012) doi:10.3791/3566.

118. Lasia, A. *Electrochemical Impedance Spectroscopy and Its Applications*. (Springer, 2020).

119. Lewis, C. M. *et al.* Recording Quality Is Systematically Related to Electrode Impedance. *Adv. Healthc. Mater.* **13**, (2024).

120. Hazelgrove, B. *et al.* Electrochemical impedance spectroscopy in vivo for neurotechnology and bioelectronics. *Nat. Rev. Electr. Eng.* **2**, 110–124 (2025).

121. Rohland, L. *Electrical Resistivity and Conductivity*. (2026).

122. SINGH, Y. ELECTRICAL RESISTIVITY MEASUREMENTS: A REVIEW. *Int. J. Mod. Phys. Conf. Ser.* **22**, 745–756 (2013).

123. Andreas Tsiamis. Electrical Test Structures and Measurement Techniques for the

Characterisation of Advanced Photomasks. (University of Edinburg, Edinburg, 2009).

124. Porto Cruz, M. F. *et al.* Bridging circuit modeling and signal analysis to understand the risk of crosstalk contamination in brain recordings. *Nat. Commun.* **16**, 4744 (2025).

125. Rairden, J. R., Neugebauer, C. A. & Sigsbee, R. A. Interdiffusion in thin conductor films — chromium/gold, nickel/gold and chromium silicide/gold. *Metall. Trans.* **2**, 719–722 (1971).

126. Martinez, W. E., Gregori, G. & Mates, T. Titanium diffusion in gold thin films. *Thin Solid Films* **518**, 2585–2591 (2010).

127. Pas, J. *et al.* A bilayered PVA/PLGA-bioresorbable shuttle to improve the implantation of flexible neural probes. *J. Neural Eng.* **15**, 065001 (2018).

128. Cointe, C. *et al.* Scalable batch fabrication of ultrathin flexible neural probes using a bioresorbable silk layer. *Microsystems Nanoeng.* **8**, 21 (2022).

L

Paper A

Towards High-Resolution Polymeric Neural Interfaces: A Practical Guide for Electron Beam Lithography

Hanna Karlsson-Fernberg, Maria Asplund*